Efficient Elimination of False Detections due to Sea Spikes in Coherent Radars

Anatolii A. Kononov*, Dohyung Kim, Sung-Hyun Choi, and Haksoo Kim

Abstract—This paper introduces a method for efficiently eliminating false detections in coherent radar systems due to sea spikes. The proposed method employs scan-to-scan processing over a predefined number of successive antenna scans. Processing consists of matching estimated range-azimuth-velocity centroid associated with each radar plot extracted from a set of data detected within the current scan (initial plot) with centroids of radar plots generated in the previous scans. For each initial plot, the proposed method matches radar plots using a sequence of correlation windows generated in turn for each of the predefined previous scans. Each correlation window defines a range-azimuth region, with center and extent in range and azimuth adjusted from scan-to-scan. A group of matched plots is selected from all plots falling into a correlation window; these plots meet the velocity matching condition. Only the one radar plot, which minimizes the predefined overall matching criterion, is selected from the given group of matched plots for inclusion in the set of correlated plots associated with the initial plot. For each identified set of correlated plots, an overall correlation value is computed. If the correlation value exceeds a predefined threshold, the initial plot associated with that set of correlated plots is stored in memory for further processing and visualization. Otherwise, the initial plot is retained for plot rematching with modified velocity centroids. The modified velocities provide the detection of those targets of interest that may have been missed due to ambiguous radial velocity measurements. In contrast to known methods, the proposed method minimizes the correlation window area at a given probability of falling into the window for radar plots associated with a target corresponding to an initial plot. The proposed method efficiently eliminates the false detections while maintaining reliable detection performance for targets of interest; the detection performance is essentially improved compared to known methods. Additionally, the proposed method ensures reliable target detection when radial velocity measurements are ambiguous, a situation where known methods collapse.

1. INTRODUCTION

Coherent radar systems are widely used for target detection and range/velocity measurements in the presence of clutter [1, 2]. For instance, pulsed Doppler radars such as VTS (vessel traffic services) radars or coastal surveillance radars inevitably encounter unwanted backscattered radar signals from the sea surface, usually referred to as sea clutter. Similarly, shipborne radars, whether used for navigation or surveillance purposes, contend with undesirable sea clutter.

For radars operating in maritime environments, the critical problem is to detect real objects (targets of interest) on the sea surface and distinguish them from apparent targets that are false detections caused by radar signal backscattering from the sea surface when no real objects are present. This problem is well known in the radar community [2, 3]. It is commonly noted, particularly in X-band radars, that as the size of the range resolution bin reduces, the clutter increasingly appears to contain sequences

* Corresponding author: Anatolii A. Kononov (akononov@onestx.com).

The authors are with the Research Center, STX Engine, 288, Guseong-ro, Giheung-gu, Yongin-si, Gyeonggi-do 16914, Republic of Korea.

of isolated discrete (target-like) returns that vary in time. These returns appear to arise due to burst scattering from the crests of waves just before they spill [3]. At the higher range resolutions, on the order of 5–10 m and higher, the discrete returns tend to stand well out of the background, occurring for both polarizations but most clearly evident with horizontal polarization at small grazing angles. These target-like returns are called sea spikes and are an inherent sea clutter component in high-resolution radars [3]. The occurrence rate of the sea spikes becomes higher as the sea state increases.

Thus, for coherent radars operating in maritime environments, an essential increase in false alarm rate is possible due to multiple false detections caused by the presence of sea spikes. These false detections appear on radar display as apparent targets, i.e., as detections that are not associated with real objects of interest. The apparent targets confuse radar operators and waste the computational resources of radar trackers. In case of a high occurrence rate, numerous false detections overwhelm the radar tracker, making tracking targets of interest impossible. The false detections caused by sea spikes are highly undesirable since they may severely impede radar missions and create a danger to navigation safety.

To cope with the problem in question, a method is required, which would allow eliminating with high probability the false detections caused by sea spikes and simultaneously maintaining reliable detection performance for the targets of interest.

Over the past years, several approaches have been studied to improve surface targets' detection while reducing the effect of sea spikes. Using real data, Rosenberg [4, 5] investigated sea-spikes' characterization to identify features that one can use to distinguish sea spikes from targets of interest. The approach used to discriminate sea-spikes from background sea clutter was to threshold the magnitude of the raw backscatter data in the range/time domain. The data after thresholding (detections due to discrete and persistent scattering) were used to verify the KK probability distribution function. Discrete and persistent detections were then isolated to provide more information on the underlying cause of sea spikes and answer whether the three-component mean Doppler spectrum model is suitable at high/medium grazing angles. Unfortunately, [4, 5] do not show how to use their results to design methods that provide reliable detection for targets of interest while efficiently eliminating false detections due to sea-spikes.

Duk et al. [6] investigated the use of stationary wavelet transform (SWT) to improve small target detection in medium grazing angle X-band sea clutter. In this work, the SWT decomposition performed on intensity data in range/time domain; application to the range/frequency domain left for future work. With this approach, one or more components (sub-bands) of the SWT decomposition have a higher signal-to-clutter ratio (SCR) than input data. Based on this observation, Duk et al. proposed to use a subset of SWT sub-bands to improve target detection performance. To better isolate targets and clutter, a sub-band isolation and reconstruction procedure was suggested. Since in noncoherent radars, target velocity is not known ahead of time, an entropy-based method was developed to select a subset of reconstructed sub-bands that contain the most information about the target and hence would provide the "best" improved detection performance. As demonstrated in [6] with simulated targets injected in a real clutter dataset, the proposed SWT-based approach improves detection performance for specific scenarios associated with the used dataset. However, that approach cannot eliminate false detections due to sea spikes; energy associated with sea spikes is distributed over the SWT sub-bands as that for targets of interest does. This is because radar returns caused by sea spikes exhibit many target-specific characteristics, including polarization independence [4].

Rosenberg et al. [7] studied a specific scan-to-scan processing structure for the detection of stationary targets with low SCR. The structure combines a block-wise scan-to-scan *integration*, as well as a corresponding CFAR processing stage and a binary integration stage for final detection. Though the investigated structure suppresses moving targets, its essential advantage is the capability of eliminating false detections caused by sea spikes.

Guan et al. [8] introduced an algebraic fractal structure combined with the Paretian Poisson process for modeling sea spikes duration. Some parameters of this model were found to have a potential for separating targets from sea spikes. As a result, a noncoherent target detection method was proposed in this work. When sea surface returns are obtained, the method separates sea spikes from the background sea clutter. Then, identified sea spikes are modeled by the Paretian Poisson process, and two model parameters are estimated. If the value of at least one of the estimates exceeds the corresponding CFAR

threshold, the detector claims a target's presence. Otherwise, no target is present. As pointed out in [8], the method is hard to implement in real-time. It requires a large number of samples to identify sea spikes reliably and to control CFAR thresholds accurately.

Li et al. [9] introduced a modified support vector machine (SVM) detector for small targets detection within sea clutter; the detector can control the probability of false alarm P_{fa} by adjusting two parameters. In order to discriminate target signals from background sea clutter, the proposed detector uses three target-specific features. There are at least two issues related to the use of the proposed SVM detector in radar applications. For radar systems, where the CFAR property has to be maintained for $P_{\mathrm{fa}} = 10^{-6} - 10^{-9}$ per resolution bin, the proposed SVM detector will require a large number of target-free training samples and essential computational capability. The most critical point is that this detector does not provide efficient eliminating false detections due to sea spikes. As we already mentioned above, radar returns caused by sea spikes have many target-specific characteristics. Therefore, the SVM detector will detect returns due to sea spikes as if they were the target-associated echoes.

Bell et al. [10] presented a statistical model for high-resolution surface radars' complex-valued data. The model assumes that radar returns from a single pulse per scan are arranged into a range/scan matrix representing multiple range bins and scans at a single azimuth. The clutter is modeled as being from one of two distributions: a background clutter distribution and wave clutter (sea spikes) distribution. The model was used to design a multi-hypothesis detector (TWB algorithm) that discriminates between targets, wave clutter, and background clutter using a fundamental statistical approach. The performance analysis results in [10] show that the TWB algorithm exhibits better detection performance than the CA-CFAR detector that operates on amplitude data using a spatially correlated K-distribution clutter model. However, the target and wave clutter classification performance does not validate the algorithm's capability in efficiently eliminating persistent false detections due to sea spikes.

Gallone et al. [11] noted that the pulse compression output associated with sea spikes received over a coherent processing interval (CPI) is similar to that associated with slowly moving low RCS targets. Because of this, false detections due to sea spikes cannot be eliminated within a single antenna scan, i.e., using conventional single scan detection after coherent integration. Work [11] proposed a method for filtering sea spikes by scan-to-scan correlation using Doppler information. As claimed in [11], that method is useful for reducing the effects of the sea spikes and filtering the radar echoes without negatively influencing the correct target detection and outperforms other known techniques (see references in [11]). However, as will be proven herein, the method suggested in [11] has the following essential disadvantages:

D1. Degradation of detection performance for targets of interest due to incorrect determination of the range extent for the range-azimuth correlation windows.

D2. Degradation of detection performance for targets of interest due to the low precision of the suggested radial velocity estimator.

D3. The angular extent of correlation windows is determined by the predefined maximum speed of targets of interest; the method does not use the estimates of azimuth centroids associated with correlated plots in adjusting the angular extent. As will be shown further, using these estimates allows reducing the said angular extent providing, thereby, the corresponding reduction in the number of false detections.

D4. Collapse of target detection performance in the case of ambiguous radial velocity measurements.

The purpose of the present paper is to develop a method for eliminating undesirable false detections associated with spiky returns caused by sea spikes using a new scan-to-scan processing technique. In this paper, we prove that the proposed new method overcomes the drawbacks of known methods and ensures:

- Better performance in eliminating the false detections than that of the known methods.

- Efficient eliminating the false detections with no negative influencing the detection performance for targets of interest.

- Capability of maintaining reliable detection performance for targets of interest even when radial velocity measurements are ambiguous.

The remaining part of this paper is organized as follows. Section 2 analyzes the disadvantages of the state-of-the-art method proposed in [11] and discusses the new method's motivations. Section 3 provides a general description (a detailed one is in the Appendix) of the proposed method and analyzes its performance. The conclusion is given in Section 4.

2. ANALYSIS OF A KNOWN STATE-OF-THE-ART METHOD

The method [11] includes two primary operations: estimation of the radial speed of radar echoes, be them targets or spikes, and scan-to-scan correlation using the radial speed estimates for the filtering sea spikes.

According to [11], the radial speed estimation is based on radar coherence and is subdivided into the following procedures:

- Dividing the radar area into discrete range intervals defining the so-called radar cells.
- Computing the phase difference $\Delta\phi$ for each radar cell between any two subsequent sweeps within a predefined coherent processing interval (CPI) comprising a multiplicity of subsequent sweeps.
- For each radar cell, computing instantaneous absolute radial speed v of the echoes as

$$v = \frac{\lambda}{4\pi T}\Delta\phi \qquad (1)$$

  where λ is the radar wavelength, T is the pulse repetition interval (PRI), i.e., the time interval between two subsequent sweeps.
- For each radar cell, averaging the radial speed values computed from Equation (1) to obtain the average radial speed V.

The scan-to-scan correlation with the use of the estimated radial speed V is carried out at the level of plots generated by the radar extractor, as disclosed in [11]:

- All plots extracted at each scan are stored in memory.
- For each extracted plot with range R and azimuth A, a range-azimuth window is defined as follows:
  i) The half azimuth extent of the window LA_a is calculated using the maximum speed $V_{\max}$ that targets of interest can reach for a specific sea state as

$$LA_a = \mathrm{asin}(V_{\max}T_{scan}/R) \qquad (2)$$

  where T_{scan} is the scanning time interval of the radar antenna.
  ii) The half range extent of the window is

$$LR_a = \alpha_w\sqrt{\sigma_R^2 + \sigma_V^2 T_{scan}^2} \qquad (3)$$

  where $\alpha_w = 3$, σ_R^2 is the variance of range estimation error, and σ_V^2 is the variance of the average velocity estimation error.
  iii) The radial position R_b of the window center is calculated as

$$R_b = R - VT_{scan} \qquad (4)$$

  where the average radial velocity V is positive if the target moves away from the radar and negative in the case of the target approaching the radar.
  iv) The azimuth center position of the window is the same as that of the plot

$$A_b = A. \qquad (5)$$

The window (or correlation window) specified above by Eqs. (2)–(5) is used to match in position and velocity the plot of the current radar scan with all the plots stored in the previous scan, some of which may fall into the window. If the correlation value, with at least one plot of the previous scan, is above a predefined threshold, then the current plot is stored for further processing and visualization on a radar display; otherwise, the current plot is canceled. Unfortunately, the description in [11] does not explain how to compute "the correlation value" for radar plots and the "predefined threshold."

In Section 1, we pointed out the disadvantages of the method proposed in [11]; in this section, we discuss them in detail.

2.1. Disadvantage D1

The half range extent of the correlation window given by formula (3) is incorrect because it ignores the range estimation errors for the plots in the previous scan. It should be noted that the range, velocity, and azimuth measurement errors are statistically independent at different scans. These errors must be taken into account because the estimated range centroid (range coordinate of the "center of gravity") of plots from the previous scan is used in the plot matching process. The plot's range (as well as velocity and azimuth) estimates $\hat{R}_n$ in any n-th scan are unbiased and belong to a measurement uncertainty interval

$$\mathcal{R}_n = [R_n - \alpha_e \sigma_R, \ R_n + \alpha_e \sigma_R] \tag{6}$$

where R_n is the actual range of a target, σ_R the standard deviation of measurement errors, and the parameter $\alpha_e > 0$ is associated with some high (close to unity) probability P_{α_e} that $\hat{R}_n \in \mathcal{R}_n$, or, in other words, measurement errors are in the interval $[-\alpha_e \sigma_R, \ \alpha_e \sigma_R]$. As well known, in the case of Gaussian-distributed errors $P_3 = 0.997300$ for $\alpha_e = 3$ and $P_4 = 0.999937$ for $\alpha_e = 4$.

Figure 1(a) shows why the half range extent given by Eq. (3) is not adequate in terms of the radar plot matching. As one can see, the full range extent of the window $[R_b - 3\sigma_R, \ R_b + 3\sigma_R]$, which is associated with some range estimates $\hat{R}_n \in \mathcal{R}_n = [R_n - 3\sigma_R, \ R_n + 3\sigma_R]$ in the n-th scan, does not cover the hatched subinterval within the interval $\mathcal{R}_{n-1} = [R_{n-1} - 3\sigma_R, \ R_{n-1} + 3\sigma_R]$ in the $(n-1)$-th scan. Therefore, for any estimate $\hat{R}_n \in \mathcal{R}_n$, there always exist estimates $\hat{R}_{n-1} \in \mathcal{R}_{n-1}$ that do not fall, with some probability, into the corresponding window (a small black square in Figure 1(a) is an example of such estimates). Obviously, radar plots associated with these estimates will be excluded from the plot matching process. Thus, using the half range extent defined in Eq. (3) may result in a low probability of correct matching, and finally, in decreasing the probability of target detection.

The probability of correct matching in range (velocity/azimuth) is said to be the probability of falling the range (velocity/azimuth) centroid of a target associated plot in the $(n-k)$-th scan, where $k \in \{1, 2, \ldots\}$ into the range (velocity/azimuth) interval of the correlation window determined using the range (velocity/azimuth) centroid of a plot associated with the same target in the n-th scan.
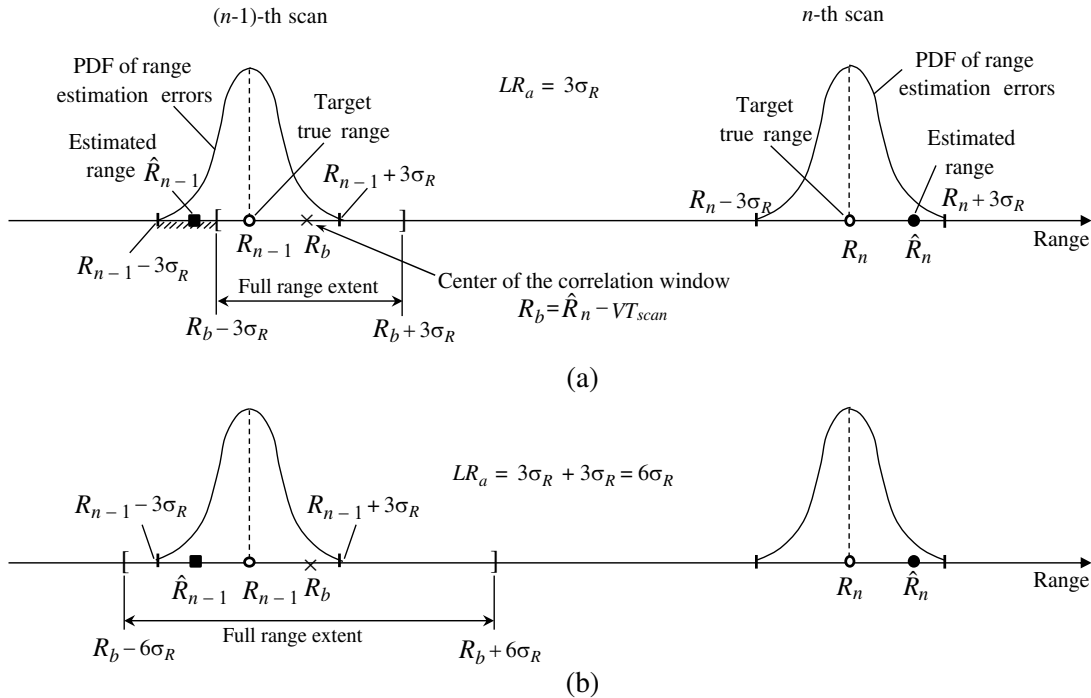
Figure 1. Determining the range extent of correlation windows ($\sigma_V^2 = 0$, for simplicity, and $\alpha_e = 3$). (a) Half range extent $LR_a = 3\sigma_R$ suggested in [11]. (b) Half range extent $LR_a = 3\sigma_R + 3\sigma_R = 6\sigma_R$ proposed in this paper.

For the Gaussian distribution of measurement errors, the probability of correct matching P^{cm} is given by

$$
\begin{aligned}
P^{\mathrm{cm}} &= \lim_{\alpha_e \to \infty} \left(\int_{-\alpha_e}^{\alpha_e} \frac{1}{\sqrt{2\pi}} \exp\left(-0.5x^2\right) \left[\int_{\max(-\alpha_e, x-\alpha_w)}^{\min(\alpha_e, x+\alpha_w)} \frac{1}{\sqrt{2\pi}} \exp\left(-0.5y^2\right) dy \right] dx \right) \\
&= \int_{-\infty}^{\infty} \frac{1}{\sqrt{2\pi}} \exp\left(-0.5x^2\right) \left[\int_{x-\alpha_w}^{x+\alpha_w} \frac{1}{\sqrt{2\pi}} \exp\left(-0.5y^2\right) dy \right] dx
\end{aligned}
\tag{7}
$$

where the parameter α_w defines the half extent (in range, velocity, or azimuth) of the corresponding correlation window.

Using Equations (7) and (3) with $\sigma_V = 0$ yields the probability of correct matching in range, i.e., in one coordinate for the method suggested in [11]

$$
P^{\mathrm{cm}} = \int_{-\infty}^{\infty} \frac{1}{\sqrt{2\pi}} \exp\left(-0.5x^2\right) \left[\int_{x-3}^{x+3} \frac{1}{\sqrt{2\pi}} \exp\left(-0.5y^2\right) dy \right] dx = 0.9661052
\tag{8}
$$

The plot matching process modifies (decreases) the probability of detections in the scans preceding the current scan in which the initial plot is selected. If a target is detected with some fixed probability P_{D} in each of the N_{s} successive scans, then the modified probability of detection after performing the plot matching (in the preceding scans) is given by

$$
P_{\mathrm{D}}^{\mathrm{mod}} = (P^{\mathrm{cm}})^d P_{\mathrm{D}}
\tag{9}
$$

where the parameter d is the number of coordinates for which the plot matching is performed, and P_{D} is the single scan detection probability determined by a CFAR method in use. Formula (8) assumes that the events of correct matching in different coordinates are independent and have the same probability.

We can simply evaluate the detection performance degradation due to the plot matching in the case of multiscan detection that uses the principle of binary integration known as the "m-of-n" rule. Consider a detection strategy when for any fixed plot, generated in the n-th current scan, one performs the plot matching process over $n = N_s - 1$ previous scans and claims the final target detection if there are at least $m = N_m - 1$ correlated plots in addition to the initial fixed plot in the n-th current scan. By correlated plots, we understand the correctly matched plots associated with the same target of interest with high probability. Thus, we observe a sequence of $N_s - 1$ statistically independent events wherein the probability of "success" (detection and correct matching) is $P_{\mathrm{D}}^{\mathrm{mod}}$ and the probability of "failure" is $1 - P_{\mathrm{D}}$ because the probability of miss is not affected by the plot matching process. For this detection strategy, the overall probability of detection is given by

$$
P_{\mathrm{D}}^{\mathrm{fin}}\left(N_m - 1 \text{ of } N_s - 1 | 1\right) = P_{\mathrm{D}} \cdot \sum_{i=N_m-1}^{N_s-1} \frac{(N_s-1)!}{i!\,(N_s-1-i)!} \left(P_{\mathrm{D}}^{\mathrm{mod}}\right)^i (1-P_{\mathrm{D}})^{N_s-1-i}
\tag{10}
$$

where the notation $P_{\mathrm{D}}^{\mathrm{fin}}(N_m - 1 \text{ of } N_s - 1 | 1)$ means the final detection probability for the detection strategy with the fixed first detection in the n-th current scan, and $N_m - 1$ is the threshold for the number of detected and correctly matched plots within the $N_s - 1$ successive previous scans.

Replacing in Eq. (10) $P_{\mathrm{D}}^{\mathrm{mod}}$ with P_{D} yields the overall detection probability under the assumption that the plot matching does not decrease the single scan detection probability

$$
P_{\mathrm{Dub}}^{\mathrm{fin}}\left(N_m - 1 \text{ of } N_s - 1 | 1\right) = P_{\mathrm{D}} \cdot \sum_{i=N_m-1}^{N_s-1} \frac{(N_s-1)!}{i!\,(N_s-1-i)!} P_{\mathrm{D}}^i (1-P_{\mathrm{D}})^{N_s-1-i}
\tag{11}
$$

For the detection strategy under consideration, $P_{\mathrm{Dub}}^{\mathrm{fin}}(N_m - 1 \text{ of } N_s - 1 | 1)$ in Eq. (11) is the upper bound for the overall probability of detection given by Eq. (10). Using Equations (10) and (11), one can present the loss in the overall detection probability as

$$
L_{\mathrm{D}}^{\mathrm{fin}}\left(N_m - 1 \text{ of } N_s - 1 | 1\right) = 1 - \frac{P_{\mathrm{D}}^{\mathrm{fin}}\left(N_m - 1 \text{ of } N_s - 1 | 1\right)}{P_{\mathrm{Dub}}^{\mathrm{fin}}\left(N_m - 1 \text{ of } N_s - 1 | 1\right)}
\tag{12}
$$

From Eqs. (8)–(12), assuming $P_D = 0.8$, $d = 3$ (plot matching in range, velocity, and azimuth) $N_s = 6$ and $N_m = 4$, we get in turn $P_D^{mod} = 0.7213784$, P_D^{fin} (3 of 5|1) $= 0.4930496$, P_{Dup}^{fin} (3 of 5|1) $= 0.7536640$, and the loss in the overall probability of detection for the method in [11]

$$L_D^{fin} (3 \text{ of } 5|1) = 1 - \frac{0.4930496}{0.7536640} = 0.3457966 \tag{13}$$

Hence, for the method proposed in [11], the loss in the overall probability of detection for targets of interest reaches an essentially high level of 34.6%.

Even if we set $d = 2$, assuming $P^{cm} = 1$ for the plot matching in azimuth since the method in [11] employs a vast azimuth extent of the correlation windows, then we get $P_D^{mod} = 0.7466874$, P_D^{fin}(3 of 5|1) $= 0.5675895$, and the loss in the overall probability of detection

$$L_D^{fin} (3 \text{ of } 5|1) = 1 - \frac{0.5675895}{0.7536640} = 0.2468932 \tag{14}$$

Thus, contrary to the statement in [11], one can conclude that the method suggested in [11] is *not free of noticeable harmful influencing the detection performance for targets of interest.*

2.2. Disadvantage D2

For the sake of clarity, in this discussion, we consider only the SIR-dependent component of the total variance of estimation errors; this component is usually the dominant one. The abbreviation SIR may represent the signal-to-noise ratio (SNR) or the signal-to-noise plus clutter ratio (SNCR).

This disadvantage appears because the estimator in Eq. (1) uses the phase difference $\Delta\phi$ measured for each radar cell at the level of raw CPI data, i.e., before coherent Doppler processing.

First, consider the radial velocity measurements in the presence of the receiver thermal noise. In this case, for the variance σ_v^2 of the velocity estimator in Eq. (1), we have [1, p. 697]

$$\sigma_v^2 \sim 1/SNR_1 \tag{15}$$

where SNR_1 is the signal-to-noise ratio for a target signal at the level of raw CPI data. Having N consecutive sweeps in CPI, one can compute the average radial velocity V using maximum $\lfloor N/2 \rfloor$ statistically independent estimates of v, where $\lfloor x \rfloor$ stands for the nearest smaller integer to x. Therefore, for the variance of the average radial velocity σ_V^2, one has

$$\sigma_V^2 \sim 1/(\lfloor N/2 \rfloor SNR_1) \tag{16}$$

In the case of coherent Doppler processing implemented as a bank of Doppler filters using Fast Fourier Transform (FFT), the SNR after coherent integration is $NSNR_1$. Accordingly, the variance of a radial velocity estimator based on fine Doppler estimation after coherent integration is

$$\sigma_V^2 \sim 1/(NSNR_1) \tag{17}$$

Therefore, in the presence of thermal noise only, the variance of the radial velocity estimator that employs fine Doppler estimation after coherent integration is half of that for the radial velocity estimator suggested in [11].

Next, consider radial velocity measurements in the presence of sea clutter. In the raw CPI data, returns from targets of interest as well as sea spikes are corrupted by the receiver thermal noise and by two continuous sea clutter components. These clutter components are the result of two scattering phenomena that are distinct from that for the sea spikes representing discrete spiky components. These phenomena are [3, p. 29–32]: a) resonant scattering from small ripples riding on top of longer ocean waves, and b) scattering from the very rough whitecaps of broken waves.

In the presence of two continuous sea clutter components mentioned above, the resulting SCNR at the level of raw CPI data may be substantially lower than the SNR. Hence, the variance σ_v^2 of the velocity estimator in Eq. (1), and respectively the variance σ_V^2 of the average velocity estimator in Eq. (16), may increase significantly. On the contrary, the resulting SCNR at the output of one of the Doppler filters (which is closely tuned to the target radial velocity) is substantially higher than that in the raw CPI data, especially for moving targets when the separation between the spectrum of a target signal and that of the continuous clutter components is large enough.

One should recall that the methods in question have to operate in scenarios when the sea spikes and two continuous clutter components are present simultaneously. Thus, the radial velocity estimator employing fine Doppler measurements is essentially more precise than suggested in [11], just in situations in which the methods in question are designed to operate.

2.3. Disadvantage D3

As follows from Eq. (2), the method [11] computes the half azimuth extent LA_a of the correlation window (for matching the current scan plots with plots stored in the previous scan) using the maximum speed $V_{\max}$ that targets of interest can reach for a specific sea state. However, the estimator in Eq. (2) can be improved using an estimate of the absolute value of the maximum tangential (cross-range) velocity $|V_{\mathrm{crmax}}|$

$$|V_{\mathrm{crmax}}| = \sqrt{V_{\max}^2 - \check{V}^2} \tag{18}$$

where $\check{V} = |V| - 6\sigma_V$, if $|V| > 6\sigma_V$, and $\check{V} = 0$, if $|V| \le 6\sigma_V$ with σ_V being the standard deviation of the estimator of velocity centroid (velocity centroider).

Using $|V_{\mathrm{crmax}}|$ from Eq. (18) yields the following improved estimator

$$LA_{ai} = \mathrm{atan}(|V_{\mathrm{crmax}}| \cdot T_{scan}/\check{R})) + 3\sigma_\alpha \tag{19}$$

where $\check{R} = R_b - LR_a$, if $R_b > LR_a$, and $\check{R} = R_b$, if $0 < R_b \le LR_a$, where LR_a is computed from Equation (48) below that correctly defines this parameter in contrast to Eq. (3), and σ_α is the standard deviation of the estimator of azimuth centroid (angular centroider). If $LA_{ai} < LA_a$, then using the estimator in Eq. (19) leads to reducing the area of the correlation window. In turn, this reduction results in decreasing the number of false detections due to sea spikes.

As will be shown further, the improved estimator in Eq. (19) provides a noticeable decrease in the number of false detections when the absolute value of the estimated radial velocity $|V|$ is close to the maximum speed $V_{\max}$. For low values of $|V|$ this estimator provides no meaningful improvements.

However, one can achieve an essential decrease in the number of false detections using the azimuth centroids of correlated plots in the plot matching process. The possibility of using the angular coordinates of these plots appears as soon as the first correlated plot is found in one of the previous scans.

Let $P_n(R, V, \alpha)$ denote a plot generated at the n-th scan. In this notation, R, V, and α are the estimated coordinates of the plot's centroid in range, velocity, and azimuth, respectively. The parameter α is a continuous circular variable, $0 \le \alpha < N_{az}$, where N_{az} is the maximum azimuth cell index within the full antenna scan.

The i-th plot $P_{ni}(R_i, V_i, \alpha_i)$, generated in the n-th current scan, and the j-th plot $P_{n-1j}(R_j, V_j, \alpha_j)$, generated in the $(n-1)$-th scan, constitute a pair of the correlated plots if they are associated (with high probability) with the same target. For a target associated with this pair of plots P_{ni} and P_{n-1j}, one can use the following estimator of the azimuth velocity $\Delta\tilde{\alpha}_{cr}$

$$\Delta\tilde{\alpha}_{cr} = \frac{(\alpha_i - \alpha_j)_{N_{az}}}{|n_i - n_j|} \frac{azimuth\ cells}{scan} \tag{20}$$

where n_i and n_j are the indices of scanning the i-th and j-th plots respectively associated with, and the notation $(\cdot)_{N_{az}}$ denotes reduction modulo N_{az} onto $[0, N_{az})$. In Matlab notation, this operation is given by $(\alpha)_{N_{az}} = mod(\alpha, N_{az})$. From Eq. (20), we get for the plots P_{ni} and P_{n-1j}

$$\Delta\tilde{\alpha}_{cr} = \frac{(\alpha_i - \alpha_j)_{N_{az}}}{|n - (n-1)|} = (\alpha_i - \alpha_j)_{N_{az}} \frac{azimuth\ cells}{scan} \tag{21}$$

Using Eq. (21) yields the azimuth coordinate α_b of the center of a new correlation window for the $(n-2)$-th scan as

$$\tilde{\alpha}_b = (\alpha_j - \Delta\tilde{\alpha}_{cr})_{N_{az}} \tag{22}$$

We assume unbiased and precise azimuth measurements for which $\sigma_\alpha \ll \theta_3$, where θ_3 is the 3 dB antenna beamwidth. Ignoring the wrapping effect of estimates within the interval $(\alpha - \theta_3, \ \alpha + \theta_3)$ for any actual

value of α, we can find the variance σ_A^2 of the estimator in Eq. (22) using its linear form $\alpha_b = 2\alpha_j - \alpha_i$. Since α_i and α_j are statistically independent, we get

$$\sigma_A^2 = 5\sigma_\alpha^2 \tag{23}$$

where σ_α^2 is the variance of the azimuth centroider.

Using Eq. (21), one can also get the azimuth coordinate $\tilde{\alpha}_b$ of the center of a new correlation window for the $(n-3)$-th scan as

$$\tilde{\alpha}_b = (\alpha_j - 2\Delta\tilde{\alpha}_{cr})_{N_{az}} \tag{24}$$

and then using the linear form of Eq. (24) $\alpha_b = 3\alpha_j - 2\alpha_i$, the corresponding variance as

$$\sigma_A^2 = 13\sigma_\alpha^2 \tag{25}$$

For targets detected with a probability of detection $P_D \geq 0.7$ (for the probability of false alarm $P_{FA} = 10^{-5}\ldots10^{-8}$), the SNR is high enough so that the standard deviation σ_α can be expected to be $\sigma_\alpha = \beta\theta_3 \approx \theta_3/10\ldots\theta_3/5$ [1, p. 703]. Then, considering the azimuth estimation errors, we obtain (by analogy with the half range extent as given by Eq. (48) below) the half azimuth extent of a new correlation window for the $(n-2)$-th scan as

$$LA_a^{adp} = 3\sigma_A + 3\sigma_\alpha = 3\left(\sqrt{5}+1\right)\sigma_\alpha \approx \begin{cases} \theta_3, & \text{for } \sigma_\alpha = \theta_3/10\,(\beta = 0.1) \\ 2\theta_3, & \text{for } \sigma_\alpha = \theta_3/5\,(\beta = 0.2) \end{cases} \tag{26}$$

and the half-azimuth extent of a new correlation window for the $(n-3)$-th scan as

$$LA_a^{adp} = 3\sigma_A + 3\sigma_\alpha = 3\left(\sqrt{13}+1\right)\sigma_\alpha \approx \begin{cases} 1.5\theta_3, & \text{for } \sigma_\alpha = \theta_3/10 \\ 3\theta_3, & \text{for } \sigma_\alpha = \theta_3/5 \end{cases} \tag{27}$$

The said new correlation window is referred to as an *adaptive correlation window* (ACW). For an ACW, the location of its center changes from scan to scan depending on the estimates of the target's radial and angular velocity. The range and azimuth extents of the ACW also change from scan to scan depending on the precision of range, velocity, and azimuth centroiders.

As follows from Eqs. (26) and (27), the full azimuth extent of the adaptive correlation window is 2–6 azimuth resolution bins. Typically, the antenna beamwidth θ_3 corresponds to N_{sw} azimuth cells, where N_{sw} is the number of sliding windows in azimuth. Therefore, the variances in Eqs. (23) and (25) can respectively be presented in terms of azimuth cells as

$$\sigma_A^2 = \begin{cases} 0.05N_{sw}^2, & \text{for } \sigma_\alpha = \theta_3/10 \\ 0.2N_{sw}^2, & \text{for } \sigma_\alpha = \theta_3/5 \end{cases} \tag{28}$$

and

$$\sigma_A^2 = \begin{cases} 0.13N_{sw}^2, & \text{for } \sigma_\alpha = \theta_3/10 \\ 0.52N_{sw}^2, & \text{for } \sigma_\alpha = \theta_3/5 \end{cases} \tag{29}$$

The half azimuth extent in Eqs. (26) and (27) is respectively in terms of azimuth cells

$$LA_a^{adp} = \begin{cases} N_{sw}, & \text{for } \sigma_\alpha = \theta_3/10 \\ 2N_{sw}, & \text{for } \sigma_\alpha = \theta_3/5 \end{cases} \tag{30}$$

and

$$LA_a^{adp} = \begin{cases} 1.5N_{sw}, & \text{for } \sigma_\alpha = \theta_3/10 \\ 3N_{sw}, & \text{for } \sigma_\alpha = \theta_3/5 \end{cases} \tag{31}$$

Figures 2(a) and 2(b) show the adaptive correlation windows for the plot matching process in the $(n-2)$-th and the $(n-3)$-th scans, respectively. The parameters of ACWs are determined using the pair of correlated plots P_{ni} and P_{n-1j}.

Equations (26), (30) and (27), (31) define the half azimuth extents for adaptive correlation window in the case when the estimator of the angular velocity uses azimuth centroids of plots from adjacent scans, i.e., from the n-th and the $(n-1)$-th scans as given by Eq. (21). Generally, if the said estimator
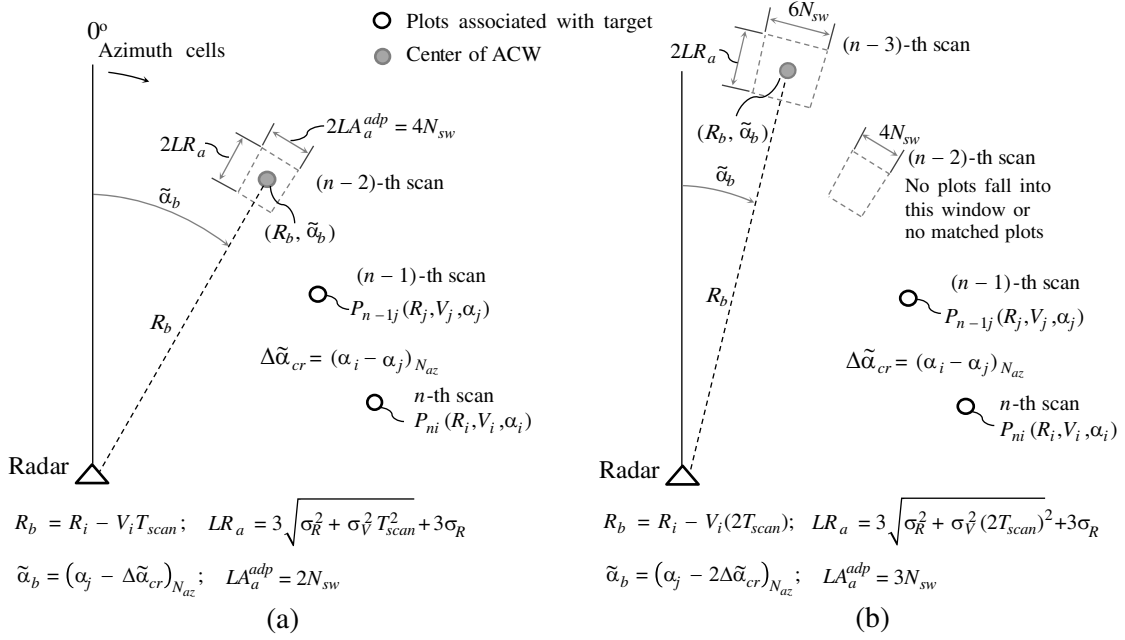
Figure 2. Determining the parameters of adaptive correlation windows using a pair of correlated plots in the $(n-1)$-th and the n-th scans: (a) for the $(n-2)$-th scan, (b) for the $(n-3)$-th scan.

employs the azimuth estimates from the n-th and the $(n-d)$-th scans, then using Eqs. (20) and (22) yields the center of the ACW in the $(n-d-h)$-th scan, $h \in [1, 2, \ldots, N_s - 1 - d]$, as

$$\tilde{\alpha}_b = \left(\alpha_j - h \frac{(\alpha_i - \alpha_j)_{N_{az}}}{d} \right)_{N_{az}} \tag{32}$$

Using the linear form of the estimator in Eq. (32) yields its variance as

$$\sigma_A^2 = \frac{(d+h)^2 + h^2}{d^2} \sigma_\alpha^2 \tag{33}$$

and in terms of azimuth cells as

$$\sigma_A^2 = \begin{cases} 0.01 N_{sw}^2 \dfrac{(d+h)^2 + h^2}{d^2}, & \text{for } \sigma_\alpha = \theta_3/10 \\[2mm] 0.04 N_{sw}^2 \dfrac{(d+h)^2 + h^2}{d^2}, & \text{for } \sigma_\alpha = \theta_3/5 \end{cases} \tag{34}$$

As follows from Eq. (33), for $d = 2$ and $h = 1$

$$\sigma_A^2 = \frac{10}{4} \sigma_\alpha^2 \tag{35}$$

and, from Eq. (34), in terms of azimuth cells

$$\sigma_A^2 = \begin{cases} 0.025 N_{sw}^2, & \text{for } \sigma_\alpha = \theta_3/10 \\ 0.1 N_{sw}^2, & \text{for } \sigma_\alpha = \theta_3/5 \end{cases} \tag{36}$$

Then, the half azimuth extent of the ACW for the $(n-d-1)$-th scan $(d = 2)$ is

$$LA_a^{adp} = 3\sigma_A + 3\sigma_\alpha = 3 \left(\frac{\sqrt{10}}{2} + 1 \right) \sigma_\alpha \approx \begin{cases} 0.8\theta_3, & \text{for } \sigma_\alpha = \theta_3/10 \\ 1.6\theta_3, & \text{for } \sigma_\alpha = \theta_3/5 \end{cases} \tag{37}$$

and in terms of azimuth cells

$$LA_a^{adp} = \begin{cases} 0.8 N_{sw}, & \text{for } \sigma_\alpha = \theta_3/10 \\ 1.6 N_{sw}, & \text{for } \sigma_\alpha = \theta_3/5 \end{cases} \tag{38}$$

Similarly, for the center of the ACW in the $(n - d - 2)$-th scan $(d = 2)$, we have

$$\tilde{\alpha}_b = \left(\alpha_j - 2 \frac{(\alpha_i - \alpha_j)_{N_{az}}}{d} \right)_{N_{az}} \tag{39}$$

and the variance of the linear version of the estimator in Eq. (39) is

$$\sigma_A^2 = \frac{(d+2)^2 + 4}{d^2} \sigma_\alpha^2 \tag{40}$$

As one can see, Eq. (40) follows from Eq. (33) with $h = 2$. Therefore, from Eq. (33), for $d = h = 2$, and from Eq. (40), for $d = 2$, we get the same result

$$\sigma_A^2 = 5\sigma_\alpha^2 \tag{41}$$

and in terms of azimuth cells

$$\sigma_A^2 = \begin{cases} 0.05 N_{sw}^2, & \text{for } \sigma_\alpha = \theta_3/10 \\ 0.2 N_{sw}^2, & \text{for } \sigma_\alpha = \theta_3/5 \end{cases} \tag{42}$$

Then, the half azimuth extent of the ACW for the $(n - d - 2)$-th scan $(d = 2)$ is

$$LA_a^{adp} = 3\sigma_A + 3\sigma_\alpha = 3(\sqrt{5} + 1)\sigma_\alpha \approx \begin{cases} \theta_3, & \text{for } \sigma_\alpha = \theta_3/10 \\ 2\theta_3, & \text{for } \sigma_\alpha = \theta_3/5 \end{cases} \tag{43}$$

and in terms of azimuth cells

$$LA_a^{adp} = \begin{cases} N_{sw}, & \text{for } \sigma_\alpha = \theta_3/10 \\ 2N_{sw}, & \text{for } \sigma_\alpha = \theta_3/5 \end{cases} \tag{44}$$

2.4. Disadvantage D4

For a pulsed Doppler radar, the target radial velocity can be measured unambiguously (assuming, for simplicity, a fixed radar platform) only if the actual radial velocity v' meets the condition

$$-V_{\text{uamax}} \le v' \le V_{\text{uamax}} \tag{45}$$

where $V_{\text{uamax}} = \frac{v_{ua}}{2}$ is the maximum unambiguous velocity with $v_{ua} = \frac{\lambda}{2T} = \frac{\lambda PRF}{2}$, where PRF is the pulse repetition frequency (PRF).

If the absolute value of the actual radial velocity v' exceeds the V_{uamax}, then the estimated apparent value will be $v = v' + k v_{ua}$ for some integer k such that v meets Eq. (45). Therefore, in the case of ambiguous velocity measurements, the estimated radial velocity v differs from the corresponding actual value v' by $k v_{ua}$, $k = \pm 1, \pm 2, \ldots$. Accordingly, for the estimated average radial velocity V we have $V = V' + k v_{ua}$, where V falls within $\pm V_{\text{uamax}}$.

The method proposed in [11] computes the range of the correlation window center using Eq. (4). Hence, for a target moving at an actual radial velocity V', where $|V'| > V_{\text{uamax}}$, the apparent radial position R_b of the correlation window center is

$$\begin{aligned} R_b &= R - V T_{scan} = R - \left(V' + k v_{ua} \right) T_{scan} \\ &= (R - V' T_{scan}) - k v_{ua} T_{scan} = R_b' - k v_{ua} T_{scan} \end{aligned} \tag{46}$$

As follows from Eq. (46), the difference $|R_b - R_b'| = |k v_{ua} T_{scan}|$ may substantially exceed the correlation window extent in the range $2LR_a$, where LR_a is given by Eq. (3). In this case, the actual target position does not fall into the precomputed correlation window. Therefore, no position and velocity matching occur for such a target over the predefined number of previous scans. As a result, all the detections associated with the target in the previous scans are missed. This mismatch explains why the method [11], collapses when radial velocity measurements are ambiguous.

Thus, it is desirable to develop such a new method employing scan-to-scan processing for eliminating false detections in coherent radar systems due to sea spikes that would be free of disadvantages of known techniques.

3. PROPOSED NEW METHOD

Figure 3 is an exemplary scan pattern of a surveillance radar, which looks for surface targets in azimuth and range using a fan antenna beam. The radar antenna rotates to scan the full azimuthal area around the radar (360° coverage in azimuth) and receives returns from some specified range interval for each azimuth cell in the whole coverage. The duration of the subsequent antenna scans is T_{scan}.
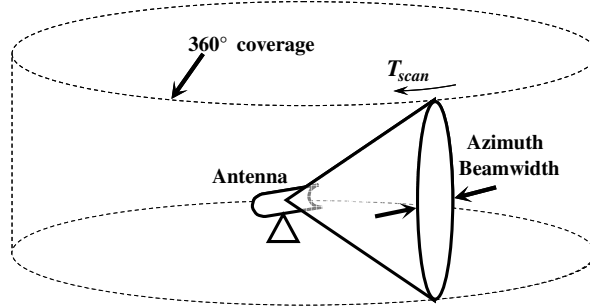
Figure 3. Scan pattern of a surveillance radar.

Figure 4 shows the full radar coverage in range and azimuth. The angular extent $\Delta\alpha_{sw}$ of an azimuth cell is equal to a fraction of the antenna beamwidth, that is $\Delta\alpha_{sw} = \theta_3/N_{sw}$, where θ_3 is the 3 dB antenna azimuth beamwidth and N_{sw} is the number of sliding windows in azimuth per the antenna beamwidth: typically, $N_{sw} = 3\ldots 6$. The duration of each sliding window in azimuth is equal to the duration of CPI. The total number of range cells is M, and the range extent ΔR (range granularity) of each range cell is typically $1/5\ldots 1/3$ of a radar range resolution δR.
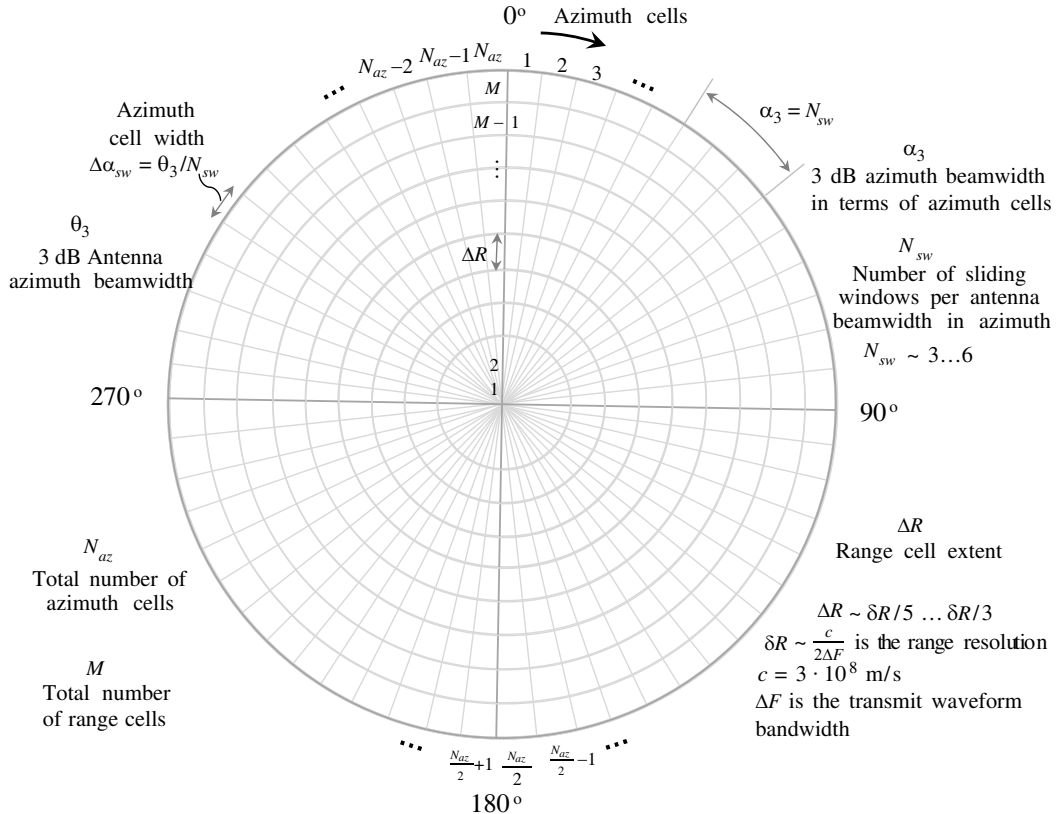
Figure 4. Full radar coverage in range and azimuth.

Radar returns received by the antenna during the CPI corresponding to each of N_{az} azimuth cells are amplified, downconverted, and digitized. After pulse compression, the digital samples are arranged into a fast/slow time (FST) complex-valued M-by-N matrix, where M is the number of range cells within the specified range interval, and N is the number of pulses transmitted within the CPI. Each row of this matrix is coherently integrated by a Doppler processor followed by a square-law detector. The Doppler processor's output is arranged into a complex-valued Range-Doppler data matrix of size M-by-N. This matrix contains all radar-available information on a specific radar scene associated with a particular azimuth cell from the full radar coverage. Further processing uses this information for target detection and measurements. The square-law detector's output is organized into an M-by-N real-valued Range-Doppler data matrix.

The proposed new method performs scan-to-scan processing over a predefined number of successive antenna scans to eliminate the false detections due to sea spikes. This processing consists of matching the estimated range-azimuth-velocity centroid associated with each radar plot extracted from a set of data detected within the current scan with centroids of radar plots generated at the previous successive scans. For each plot in the current antenna scan (initial plot), the proposed method matches the radar plots using a sequence of correlation windows generated in turn for each of the predefined previous scans. Each correlation window defines a range-azimuth region, with center and extent adjusted from scan-to-scan. These adjustments minimize the area of the correlation window under the condition that plots associated with a target corresponding to the initial plot fall into the window with high probability. A group of matched plots is selected from all plots falling into the correlation window; these plots meet the velocity matching condition. Only the one radar plot, which minimizes the predefined overall matching criterion, is selected from the given group of matched plots for inclusion in the set of correlated plots associated with the initial plot. After matching the plots over a predefined number of successive previous scans, a set of correlated plots is identified for each initial radar plot. The proposed new method performs the plot matching in two runs. The first run uses initial (computed by plot extractor) velocity centroids of plots, and the second run performs plot re-matching using modified velocity centroids. The modifications provide the detection of those targets of interest that have probably been missed due to ambiguous velocity measurements. For each identified set of the correlated plots, an overall correlation value is computed. If this value exceeds a predefined threshold, then the initial plot from the current antenna scan associated with the set of correlated plots is stored in memory for further processing and visualization. Otherwise, the set of correlated plots is retained for plot re-matching after the first run or discarded after the second run.

The positions (range-azimuth centroids) of radar plots related to sea spikes do not depend on the sea spikes' velocities; they change randomly from scan-to-scan. Hence, the overall correlation values for the plots associated with sea spikes are generally below the threshold. In contrast, radar plots related to targets of interest change their positions from scan-to-scan regularly depending on targets' velocities. Therefore, the overall correlation values for plots associated with targets to be detected are generally above the threshold. The proposed new method employs these phenomena to eliminate false detections due to sea spikes while maintaining reliable detection performance for targets of interest.

A block diagram in Figure 5 illustrates a fully coherent pulsed radar system that contains a DSP unit that implements the proposed new method. The DSP unit performs all the functions required to eliminate the false detections due to sea spikes and maintain reliable detection performance for targets of interest. In Figure 5, Section A contains typical blocks required to generate the coherent sequence of transmit waveforms, to radiate these waveforms into a specified space region, to receive and coherently process returns. For the sake of simplicity, the synchronizer that supplies the synchronizing signals needed to control timing throughout the radar system (transmitted pulses, analog-to-digital (A/D) and digital-to-analog (D/A) converter, DSP unit, radar display, and other associated circuits) is omitted. The power amplifier usually employs solid-state devices. The transmit waveform may be represented at intermediate frequency by a sequence of real samples; these samples are extracted from memory and converted into an analog signal at the waveform generator output. The acronym LNA stands for a low noise amplifier.

Figure 6 shows a block diagram of the proposed new method, wherein the input is the complex-valued FST data matrix of size M-by-N that represents raw CPI data after the pulse compression. This block diagram comprises:
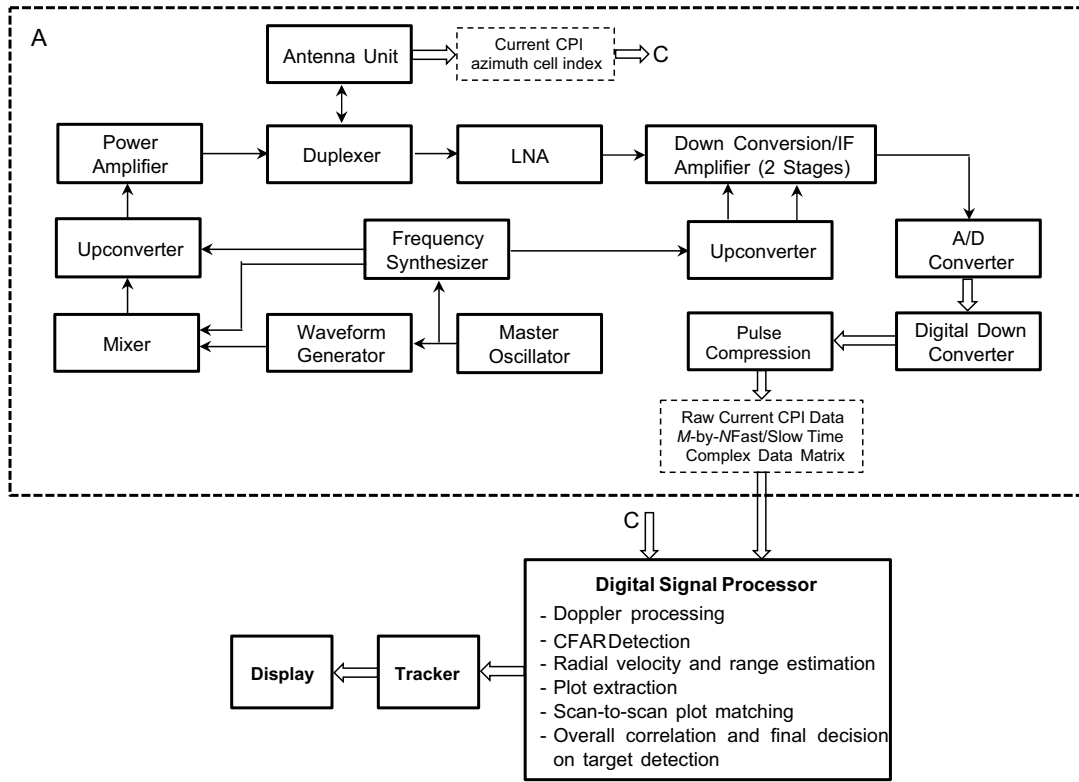
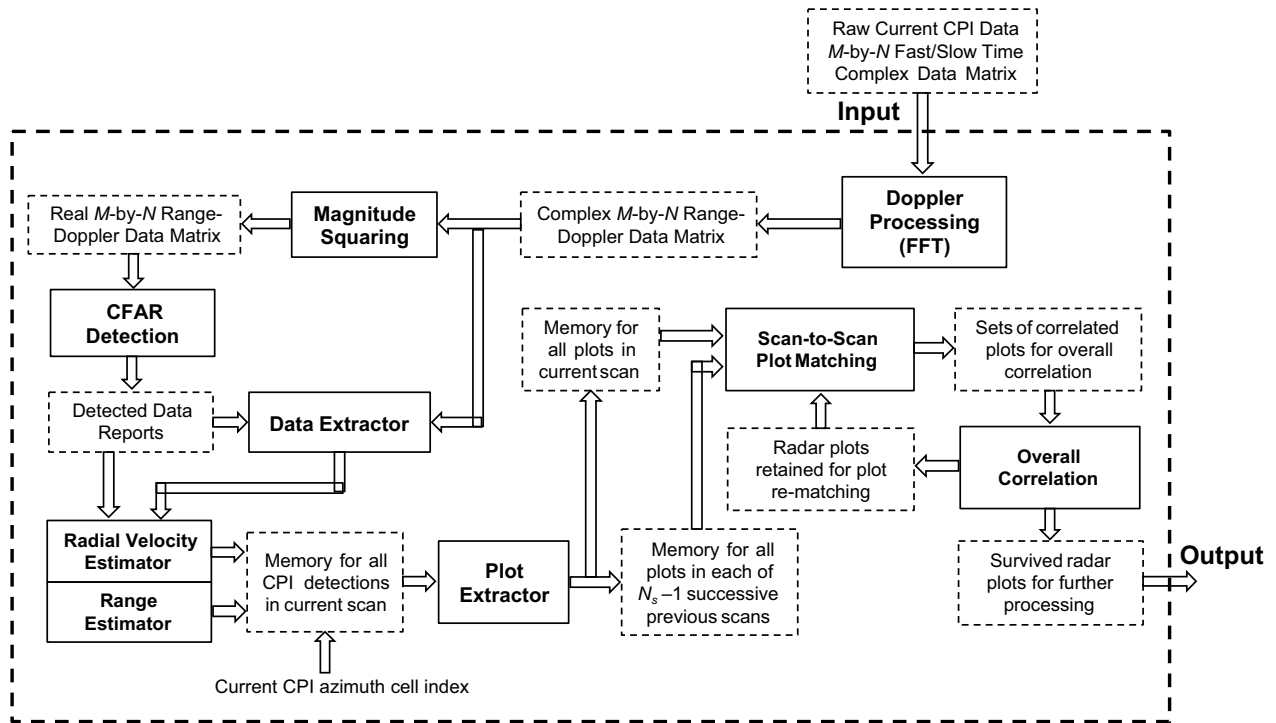**Figure 5.** Pulsed Doppler radar system with a DSP unit implementing the proposed method.

Figure 6. Block diagram of a DSP unit implementing the proposed method.

1) Computing block "Doppler Processing" for performing coherent integration of radar returns represented in the FST data matrix by applying a Fast Fourier Transform (FFT) to each row of the matrix. Doppler processing substantially improves the output SNR and SNCR relative to their corresponding input values [1, 2], especially for targets separated from the clutter in the Doppler domain. The output of Doppler processing is a complex-valued Range-Doppler data matrix of size M-by-N.

2) Computing block "Magnitude Squaring" for converting the output of Doppler processing into a real-valued Range-Doppler data matrix of size M-by-N

3) Computing block "CFAR Detection" for performing reliable target detection using as input the real-valued Range-Doppler data matrix. This block can exploit any appropriate CFAR techniques, in particular, advanced CFAR approaches introduced in [12, 13] and [14, 15]. The output of this block is Detected Data Reports that contain the range cell indices of detected samples in the real-valued Range-Doppler data matrix, as well as a value of the maximum magnitude among all Doppler samples associated with each detected range cell (i.e., such a range cell for which there is at least one detected sample) and the Doppler bin index associated with the said maximum Doppler sample.

4) Data extraction block "Data Extractor" for extracting a set of data required for fine Doppler estimation from the complex-valued Range-Doppler data matrix. The data set is extracted for each detected range cell and usually consists of the complex sample associated with the maximum Doppler sample, two neighboring complex samples, and their corresponding Doppler bin indices.

5) Computing blocks "Radial Velocity Estimator" and "Range Estimator." The former computes a radial velocity estimate (for each detected range cell) as $V = (\lambda/2)F_D$, where λ is the radar wavelength and F_D is the fine Doppler frequency estimate. Fine Doppler estimator uses a set of complex samples at the output of "Data Extractor." An example of the fine Doppler estimator operating on complex samples is given by [1, p. 520]

$$\begin{cases} f = k_0 + \Delta k = k_0 - \text{Re}\left\{ \dfrac{Y[k_0+1] - Y[k_0-1]}{2Y[k_0] - Y[k_0-1] - Y[k_0+1]} \right\} \\ F_D = \dfrac{PRF}{N}\left(f - \dfrac{N}{2} - 1 \right) \end{cases} \tag{47}$$

where f is the normalized Doppler frequency estimate; k_0 and $Y[k_0]$ is respectively the Doppler bin index and complex sample associated with the maximum sample $|Y[k_0]|$; $Y[k_0-1]$ and $Y[k_0+1]$ are the two neighboring complex samples of $Y[k_0]$; F_D is the fine Doppler frequency estimate (zero-centered) in Hertz; PRF is the pulse repetition frequency, and $N = 2^n$ ($n = 3, 4, \ldots$) is the FFT length.

The range estimator computes a range estimate for each detected range cell as $R = r\Delta R$, where r is the associated range cell index and ΔR the range cell extent in meters.

The radial velocity and range estimates computed by "Radial Velocity Estimator" and "Range Estimator," respectively, for all detected range cells within each current CPI, as well as the azimuth cell index associated with the current CPI, are accumulated in the memory over the whole current scan.

6) Computing block "Plot Extractor" for grouping the samples associated with detections occurred in the current scan into plots and estimating their centroids in range, azimuth, and radial velocity. The plots' centroids are stored in the memory for the current scan and accumulated in the memory for the $N_s - 1$ successive previous scans. A set of the plot-associated data also includes the range-azimuth samples constituting the plot and their corresponding range-azimuth cell indices.

7) Computing block "Scan-to-Scan Plot Matching" that executes, starting from each plot in the current scan(initial plot), the matching of that initial plot with plots in the $N_s - 1$ successive previous scans using estimates of their range-azimuth-velocity centroids. All the plots, which centroids meet predefined matching criteria, survive. The initial plot and all the corresponding survived plots compose a set of the correlated plots (SCP). The sets of correlated plots, the number of plots N_{cor}, and data associated with correlated plots in each SCP are stored in the memory for further processing.

8) Computing block "Overall Correlation" for computing the overall correlation value for each SCP and making decisions based on this value. If the overall correlation value is equal to or greater than a predefined threshold, then the initial plot survives, and its associated data are stored in memory for further processing and visualization. Otherwise, the initial plot is retained for the plot re-matching in block "Scan-to-Scan Plot Matching." The plot re-matching operates on retained plots using both initial and modified velocity centroids. The modified velocity centroids are computed from initial velocity centroids by shifting them to a predefined ambiguity interval in velocity. After plot re-matching, a new SCP is generated for each retained plot. If the overall correlation value for the new SCP is below a predefined threshold, the corresponding retained plot is discarded.

In particular, this block can use the "m-of-n" rule, where m is the predefined threshold for the number of correlated plots in an SCP and n is the predetermined number of the successive previous scans used in the plot matching process. If $N_{cor} \geq m$, the data set of the initial plot in the SCP is stored in the memory for further processing and visualization; otherwise, the initial plot is discarded. In the case of the "m-of-n" rule, the equivalent correlation value is N_{cor}/N_s and the equivalent correlation threshold is m/n.

In contrast to the method [11], the proposed new method considers the range estimation errors for plots in the previous scans. These errors must be considered because the plot matching procedure verifies the range matching condition using the estimated range centroids of a plot in the n-th current scan and plots in the previous antenna scan. Under the assumption that the variance of a range estimator is constant within the predefined number of scans, the corresponding equation for the half range extent LR_a of the correlation window in the $(n-1)$-th previous scan is given by

$$LR_a = \alpha_w \sqrt{\sigma_R^2 + \sigma_V^2 T_{scan}^2} + \alpha_w \sigma_R \tag{48}$$

where the parameter $\alpha_w > 0$ governs the half range extent, and the second term $\alpha_w \sigma_R$ accounts for the range estimation errors in the previous scans.

Figure 1(b) shows the benefit of the new half extent value $LR_a = 3\sigma_R + 3\sigma_R = 6\sigma_R$ computed from (48) assuming $\alpha_w = 3$ and $\sigma_V^2 = 0$. As can be seen, for a given range estimate in the n-th scan $\hat{R}_n$, the full range extent of the correlation window $[R_b - 6\sigma_R, R_b + 6\sigma_R]$ entirely covers the uncertainty interval $\mathcal{R}_{n-1} = [R_{n-1} - 3\sigma_R, R_{n-1} + 3\sigma_R]$ in the $(n-1)$-th scan. This full-coverage occurs even when the estimate $\hat{R}_n$ is equal to the upper bound $R_n + 3\sigma_R$ of the uncertainty interval $\mathcal{R}_n$ in the n-th scan. Hence, the plot associated with any range estimate $\hat{R}_{n-1} \in \mathcal{R}_{n-1}$ will never be excluded from the matching process.

Thus, the half range extent defined in Eq. (48) maximizes the probability of correct matching for a given α_w and, therefore, should not have a noticeable detrimental effect on the probability of target detection. Indeed, using Equations (7) and (48) with $\alpha_w = 3$ and $\sigma_V = 0$ yields the probability of correct matching in one coordinate for the method proposed in this paper

$$P^{cm} = \int_{-\infty}^{\infty} \frac{1}{\sqrt{2\pi}} \exp\left(-0.5x^2\right) \left[\int_{x-6}^{x+6} \frac{1}{\sqrt{2\pi}} \exp\left(-0.5y^2\right) dy\right] dx = 0.9999779 \tag{49}$$

Then, using Equations (8)–(12) with settings $P_D = 0.8$, $d = 3$, $N_s = 6$ and $N_m = 4$, we get for the proposed new method $P_D^{mod} = 0.7999470$ and, finally

$$P_D^{fin} (3 \text{ of } 5|1) = 0.7534577 \tag{50}$$

$$L_D^{fin} (3 \text{ of } 5|1) = 1 - \frac{0.7534577}{0.7536640} = 2.7369443 \times 10^{-4} \tag{51}$$

As follows from Eq. (51), for the new method, the loss in the overall probability of detection is an essentially small value of 0.0273694%, which is a practically negligible quantity. It is straightforward, using the quantities of $P_D^{fin}(3 \text{ of } 5|1)$ from Equations (13) and (51), to evaluate the loss in the overall probability of detection for the method [11] relative to the proposed new method as

$$\frac{L_D^{fin} (3 \text{ of } 5|1)}{Prior\ art\ vs\ new\ method} = 1 - \frac{0.4930496}{0.7534577} = 0.3456174 \tag{52}$$

From Eq. (52), this loss is 34.6%, i.e., as large as that for the method proposed in [11] relative to the upper bound $P_{\text{Dub}}^{\text{fin}} = 0.7536640$ computed from Eq. (11).

Thus, in contrast to the method [11], the new method is practically free of negative influencing the target detection performance. Thereby, the proposed new method provides *radically improved detection performance for targets of interest* relative to state-of-the-art methods.

The azimuth extent defined in [11] for the correlation windows is not the best choice to reduce the number of false detections due to the sea spikes. Indeed, as follows from Eq. (2), the azimuth extent $2LA_a$ of the prior art correlation window (PCW) proposed in [11] may be too large, especially for near-range targets, since it is calculated using a predefined maximum speed $V_{\max}$.

The proposed new method employs two kinds of correlation windows. The first one is referred to as the *initial correlation window*. An initial correlation window (ICW) is generated whenever the new method starts matching a plot in the current scan with plots in the adjacent previous scan; these scans are separated in time by T_{scan}. For each i-th plot $P_{ni}(R_i, V_i \alpha_i)$ in the n-th current scan, the center position of the ICW is determined as follows:

- The range R_b of the ICW center is calculated as

$$R_b = R_i - V_i T_{scan}, \tag{53}$$

  where the velocity of the centroid V_i is positive if the target moves away from the radar and negative if the target approaches the radar.

- The azimuth center of the ICW is equal to the azimuth centroid of the plot

$$A_b = \alpha_i, \tag{54}$$

- The azimuth extent of the ICW (in terms of azimuth cells) is computed using Eq. (19) as

$$LA_{ai} = \left\lceil \frac{\text{atan}(|V_{\text{crmax}}| \cdot T_{scan}/R_{\text{bmin}})}{\theta_3} \right\rceil N_{sw} + \lceil 3\beta \rceil N_{sw}, \tag{55}$$

  where $|V_{\text{crmax}}| = \sqrt{V_{\max}^2 - \check{V}^2}$ with $\check{V} = |V_i| - 6\sigma_V$ if $|V_i| > 6\sigma_V$, and $\check{V} = 0$ if $|V_i| \leq 6\sigma_V$, and $R_{\text{bmin}} = R_b - LR_a$ if $R_b > LR_a$ and $R_{\text{bmin}} = R_b$, if $0 < R_b \leq LR_a$. Here, LR_a is given by Eq. (48); β is the parameter in an expression for the standard deviation σ_α of an angular centroider ($\sigma_\alpha = \beta\theta_3$ or $\sigma_\alpha = \beta N_{sw}$), and the function $\lceil x \rceil$ returns the nearest larger integer to x.

The second kind of correlation window is referred to as the *adaptive correlation window* (ACW). Adaptive correlation windows are generated after the first correlated plot is found in the ICW. In this case, there are two azimuth centroids associated with the correlated plots. For instance, if the first correlated plot is found in the adjacent previous scan, these centroids are α_i associated with the i-th plot $P_{ni}(R_i, V_i, \alpha_i)$ in the n-th current scan, and α_j associated with the corresponding j-th plot $P_{n-1j}(R_j, V_j, \alpha_j)$ in the $(n-1)$-th scan. Then, the azimuth center of the ACW for matching the plot $P_{n-1j}(R_j, V_j, \alpha_j)$ in the $(n-1)$-th scan with the plots $P_{n-2k}(R_k, V_k, \alpha_k)$ in the $(n-2)$-th scan (i.e., in the second previous scan) is computed, taking into account that azimuth centroids are continuous circular variables on $[0, N_{az})$, as

$$\tilde{\alpha}_b = \begin{cases} \alpha_b, & \text{if } 0 \leq \alpha_b < N_{az} \\ \alpha_b - N_{az}, & \text{if } \alpha_b \geq N_{az} \\ \alpha_b + N_{az}, & \text{if } \alpha_b < 0 \end{cases} \tag{56}$$
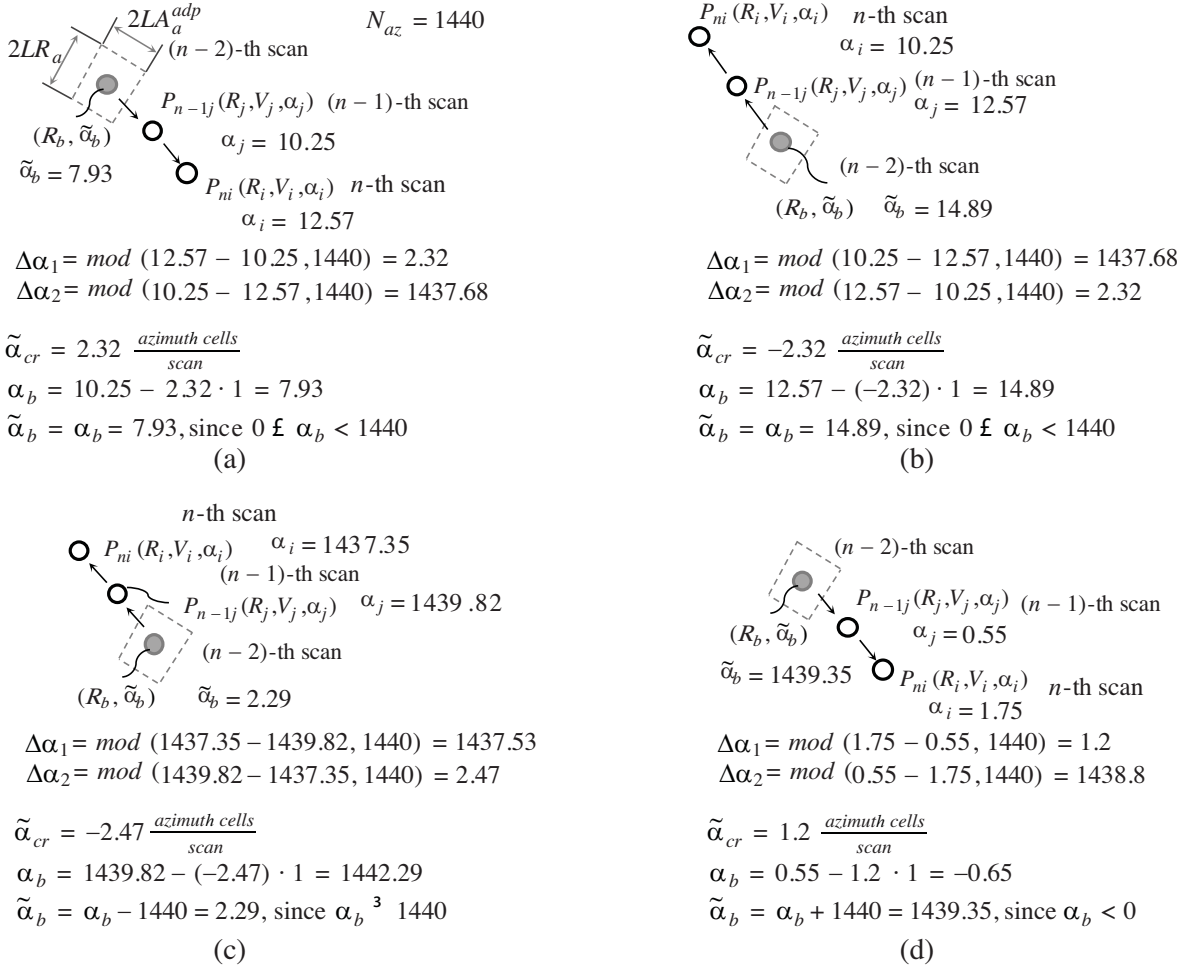
where $\alpha_b = \alpha_j - \tilde{\alpha}_{cr}$ and the azimuth velocity $\tilde{\alpha}_{cr}$ for a target associated with the plots $P_{ni}(R_i, V_i, \alpha_i)$ and $P_{n-1j}(R_j, V_j, \alpha_j)$ is computed using (20) as

$$\tilde{\alpha}_{cr} = \begin{cases} \Delta\alpha_1, & \text{if } \Delta\alpha_1 \leq \Delta\alpha_2 \\ -\Delta\alpha_2, & \text{if } \Delta\alpha_1 > \Delta\alpha_2 \end{cases} \tag{57}$$

with $\Delta\alpha_1$ and $\Delta\alpha_2$ being computed from

$$\begin{aligned} \Delta\alpha_1 &= mod(\alpha_i - \alpha_j, N_{az}) \\ \Delta\alpha_2 &= mod(\alpha_j - \alpha_i, N_{az}) \end{aligned} \tag{58}$$

where $mod(x, N_{az})$ returns the remainder after division of x by N_{az}.

Figure 7. Examples of computing the azimuth coordinate of the center of ACW.

Figure 7 shows four numerical examples of using Eqs. (56)–(58). In Eq. (57), the sign of the estimate $\tilde{\alpha}_{cr}$ defines the direction of the target's azimuth change; $\tilde{\alpha}_{cr} \geq 0$ means that the target moves "clockwise"; otherwise, it moves "anticlockwise."

Using the half azimuth extent given by Eq. (30), the azimuth correlation interval $[\tilde{A}_L, \tilde{A}_U]$ for matching the plot $P_{n-1j}(R_j, V_j, \alpha_j)$ with the plots $P_{n-2k}(R_k, V_k, \alpha_k)$ is computed as

$$\tilde{A}_L = \begin{cases} A_L, & \text{if } 0 \leq A_L < N_{az} \\ A_L - N_{az}, & \text{if } A_L \geq N_{az} \\ A_L + N_{az}, & \text{if } A_L < 0 \end{cases} \tag{59}$$

$$\tilde{A}_U = \begin{cases} A_U, & \text{if } 0 \leq A_U < N_{az} \\ A_U - N_{az}, & \text{if } A_U \geq N_{az} \\ A_U + N_{az}, & \text{if } A_U < 0 \end{cases} \tag{60}$$

where $A_L = \tilde{\alpha}_b - LA_a^{adp}$, $A_U = \tilde{\alpha}_b + LA_a^{adp}$, and according to Eq. (30), $LA_a^{adp} = 2N_{sw}$ is the half azimuth extent of the ACW to be used in matching the plots from $(n-2)$-th scan with the correlated plot found in the $(n-1)$-th scan. For this ACW, the range coordinate of the center is

$$R_b = R_j - V_j T_{scan} \tag{61}$$

To characterize the effect of the area of a range-azimuth correlation window on the number (as well as the probability) of false detections due to the sea spikes, we use the probability that at least one sea spike occurs in the range-azimuth region associated with a given correlation window. To that end,

we use a statistical model of sea spikes introduced in [3, p. 115–124]. This model assumes a Poisson distribution that describes fluctuations in a population of independent, un-bunched spikes. According to the model, the mean number of spikes in any range-azimuth resolution element (bin) is $\bar{N} \ll 1$, so that the probability of occurring m spikes in a range-azimuth bin, $P_{\mathrm{sp}}(m)$ is given by

$$
\begin{aligned}
P_{\mathrm{sp}}(0) &= 1 - \bar{N} \\
P_{\mathrm{sp}}(1) &= \bar{N} \\
P_{\mathrm{sp}}(m \geq 2) &= 0
\end{aligned}
\tag{62}
$$

The occurrences of sea spikes in a set of range-azimuth bins are independent events. Hence, the probability of occurring at least one sea spike in each range-azimuth correlation window is given by

$$
P_{\mathrm{W}}(m \geq 1) = 1 - \left(1 - \bar{N}\right)^{N_{bin}(\mathrm{W})}
\tag{63}
$$

where $N_{bin}(\mathrm{W}) = N_{bin}^{azm} \cdot N_{bin}^{rng}$ is the total number of range-azimuth bins in a given correlation window with N_{bin}^{azm} and N_{bin}^{rng} being the number of resolution bins within the azimuth and range extents of the window, respectively, and W stands for the type of window: PCW for the correlation window according to the method disclosed in [11]; ACW and ICW respectively for the adaptive and initial correlation windows according to the proposed new method.

In the comparative analysis of the false detection elimination performance, we compare the values of $P_{\mathrm{W}}(m \geq 1)$ for the PCW (method in [11]) and those for the ICW and ACW (proposed new method) under the following settings:

- Scanning time: $T_{scan} = 6\,\mathrm{s}$.
- Range interval for plots (in meters): $[R_{\min}, R_{\max}] = [100, 10000]$.
- Standard deviations: $\sigma_R = 3\,\mathrm{m}$, $\sigma_V = 0.3\,\mathrm{m/s}$ and $\sigma_\alpha = \theta_3/5 = 0.1°$.
  These parameters are SNR dependent, and the SNR is a decreasing function of range.
  It is assumed that σ_R, σ_V and σ_α correspond to a boundary SNR at point $R_{\max}$.
  Thus, for any range $R \in [R_{\min}, R_{\max}]$, given precision is guaranteed.
- Maximum speed for a target of interest: $V_{\max} = 20\,\mathrm{m/s}$ and $40\,\mathrm{m/s}$.
- Range resolution: $\delta R = 10\,\mathrm{m}$.
- Azimuth resolution: $\delta\theta_3 = \theta_3 = 0.5°$.
- Probability of occurring one sea spike in a range-azimuth bin: $P_{sp}(1) = \bar{N} = 0.01$ [3, p. 126].

In this analysis, we assume that all the correlation windows in question have the same correctly defined half range extent given by Eq. (48)

$$
LR_a = 3\sqrt{3^2 + (0.3 \cdot 6)^2} + 3 \cdot 3 = 19.5m
\tag{64}
$$

Hence, all the windows have the same number of range bins N_{bin}^{rng} within the range extent in Eq. (64)

$$
N_{bin}^{rng} = 2\frac{LR_a}{\delta R} = 2\left\lceil\frac{19.5}{10}\right\rceil = 4
\tag{65}
$$

As follows from Eq. (26), for a pair of the correlated plots P_{ni} and P_{n-1j}, the full azimuth extent of the ACW is $2LA_a^{adp} = 4\theta_3$. Therefore, the number of azimuth bins within this azimuth extent is

$$
N_{bin}^{azm} = \frac{2LA_a^{adp}}{\theta_3} = 4
\tag{66}
$$

and the total number of range-azimuth bins

$$
N_{bin}(\mathrm{ACW}) = N_{bin}^{azm} \cdot N_{bin}^{rng} = 4 \cdot 4 = 16
\tag{67}
$$

The half azimuth extent of the ACW given by Eqs. (26) and (30) depends on the precision of the azimuth centroider. Therefore, these equations define the minimum azimuth extent for other correlation windows. Thus, for the PCW and ICW, the number of azimuth bins is greater than or equal to that given by Eq. (66).

For the ICW, using the azimuth extent given by Eq. (19) and the lower bound given by Eq. (66) yields the corresponding number of azimuth bins as

$$N_{bin}^{azm} = \max\left\{\frac{\mathrm{atan}(|V_{\mathrm{crmax}}| \cdot T_{scan}/(R - LR_a)) + 3\sigma_\alpha}{\theta_3}, 4\right\} \tag{68}$$

where $|V_{\mathrm{crmax}}|$ is given by Eq. (18), and the total number of range-azimuth bins

$$N_{bin}(\mathrm{ICW}) = 4 \cdot \max\left\{\frac{\mathrm{atan}(|V_{\mathrm{crmax}}| \cdot T_{scan}/(R - LR_a)) + 3\sigma_\alpha}{\theta_3}, 4\right\} \tag{69}$$

Similarly, using Eqs. (2) and (66) yields for the PCW

$$N_{bin}(\mathrm{PCW}) = 4 \cdot \max\left\{\frac{\mathrm{asin}(V_{\mathrm{max}} \cdot T_{scan}/R)}{\theta_3}, 4\right\} \tag{70}$$

Under the assumption that the ACW parameters are computed using radar plots in the adjacent scans, the probability of occurring at least one sea spike, as follows from Eqs. (63) and (67), is a range independent constant

$$P_{\mathrm{ACW}}(m \geq 1) = 1 - (1 - 0.01)^{16} = 0.149 \tag{71}$$

Figure 8 shows the graphs of the improvement (reduction) factors Q in the probability of occurring at least one sea spike for the ICW relative to the PCW, and Figure 9 shows similar graphs for the ACW relative to the PCW and ICW. Using Eqs. (69)–(71) yields the following formulas for computing the improvement factors

For ICW relative to PCW

$$Q(\mathrm{ICW\ vs.\ PCW}) = \frac{P_{\mathrm{PCW}}(m \geq 1)}{P_{\mathrm{ICW}}(m \geq 1)} = \frac{1 - (1 - \bar{N})^{N_{bin}(\mathrm{PCW})}}{1 - (1 - \bar{N})^{N_{bin}(\mathrm{ICW})}}, \quad R \in [R_{\mathrm{min}}, R_{\mathrm{max}}] \tag{72}$$

For ACW relative to ICW

$$Q(\mathrm{ACW\ vs.\ ICW}) = \frac{P_{\mathrm{ICW}}(m \geq 1)}{P_{\mathrm{ACW}}(m \geq 1)} = \frac{1 - (1 - \bar{N})^{N_{bin}(\mathrm{ICW})}}{P_{\mathrm{ACW}}(m \geq 1)}, \quad R \in [R_{\mathrm{min}}, R_{\mathrm{max}}] \tag{73}$$

For ACW relative to PCW

$$Q(\mathrm{ACW\ vs.\ PCW}) = \frac{P_{\mathrm{PCW}}(m \geq 1)}{P_{\mathrm{ACW}}(m \geq 1)} = \frac{1 - (1 - \bar{N})^{N_{bin}(\mathrm{PCW})}}{P_{\mathrm{ACW}}(m \geq 1)}, \quad R \in [R_{\mathrm{min}}, R_{\mathrm{max}}] \tag{74}$$

The graphs of the improvement factors in Figures 8 and 9 are computed for $V_{\mathrm{max}} = 20\,\mathrm{m/s}$ and $V_{\mathrm{max}} = 40\,\mathrm{m/s}$ at $|V_r|/V_{\mathrm{max}} = 0.5$, 0.9 and 0.99. Figure 8 shows the improvement factor $Q(\mathrm{ICW\ vs.\ PCW})$ as a function of range. For $|V_r|/V_{\mathrm{max}} = 0.5$, one can observe some small degradation in this improvement factor; the degradation does not exceed 6% and 4% for $V_{\mathrm{max}} = 20\,\mathrm{m/s}$ and $V_{\mathrm{max}} = 40\,\mathrm{m/s}$, respectively. However, the ICW can provide a noticeable reduction of 50% or more ($Q \geq 1.5$) in the probability of occurring at least one sea spike when the ratio $|V_r|/V_{\mathrm{max}} \geq 0.99$ for both $V_{\mathrm{max}} = 20\,\mathrm{m/s}$ and $40\,\mathrm{m/s}$. Comparing the plots in Figure 8 for these values of V_{max} shows that the improvement factor increases for the higher value of V_{max}. For $V_{\mathrm{max}} = 40\,\mathrm{m/s}$, the "effective" range interval, i.e., the range interval within which $Q \geq 1.5$, extends up to $4300\,\mathrm{m}$, and it is two times broader than that for $V_{\mathrm{max}} = 20\,\mathrm{m/s}$.

The plots in Figure 9 show that the ACW provides a noticeable reduction in the probability of occurring at least one sea spike relative to both the ICW and the PCW. This reduction is especially prominent for $Q(\mathrm{ACW\ vs.\ PCW})$ at $V_{\mathrm{max}} = 40\,\mathrm{m/s}$. In this case, the "effective" range interval also extends up to $4300\,\mathrm{m}$ and is two times wider than that for $V_{\mathrm{max}} = 20\,\mathrm{m/s}$.

Thus, in contrast to the method [11], the proposed new method ensures a noticeable reduction in the probability of occurring at least one spike in the area occupied by adaptive correlation windows. Thereby, the proposed new method provides a *noticeable decrease in the number of false detections due to the sea spikes* relative to state-of-the-art methods.

It is also of interest to evaluate the overall probability of detection for the sea spikes using their statistical model discussed above. For a single range-azimuth resolution element, we will find this
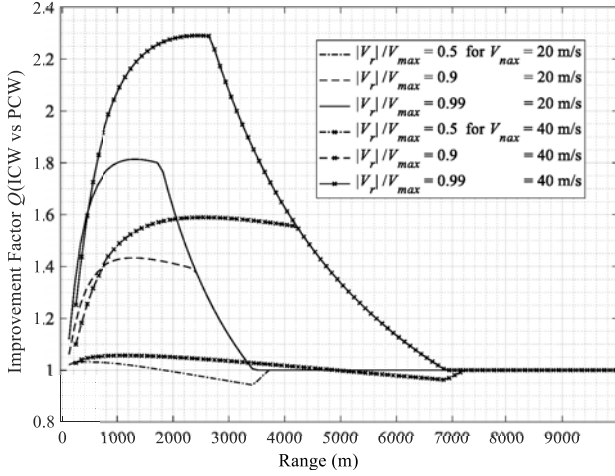
Figure 8. Improvement factor for ICW relative to PCW.
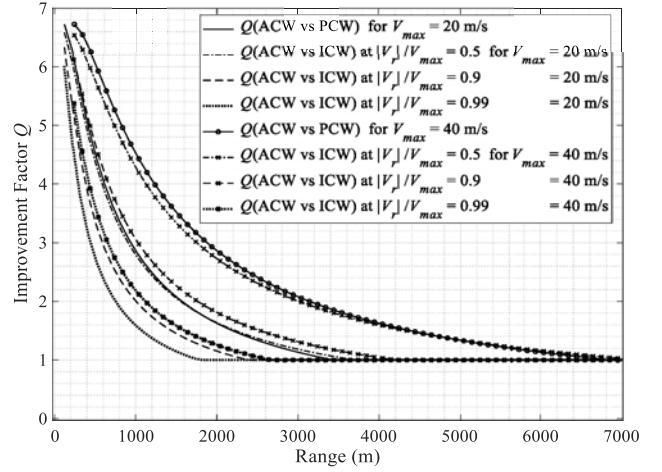
Figure 9. Improvement factor for ACW relative to PCW and ICW.

probability from Eq. (10), assuming that a sea spike that appears in the resolution element with probability $P_{\rm sp}(1)$ is detected by radar with probability unity in any single scan. We also assume ideal plot matching (probability of correct matching is unity) in all coordinates. Then, substituting in Eq. (10) $P_{\rm D}$ and $P_{\rm D}^{\rm mod}$ with $P_{\rm sp}(1)$ from Eq. (62) yields the sought probability

$$P_{\rm Dsp}^{\rm fin}\left(N_m - 1 \text{ of } N_s - 1|1\right) = P_{\rm sp}\left(1\right) \cdot \sum_{i=N_m-1}^{N_s-1} \frac{(N_s - 1)!}{i!\,(N_s - 1 - i)!}\left(P_{\rm sp}\left(1\right)\right)^i\left(1 - P_{\rm sp}\left(1\right)\right)^{N_s-1-i} \quad (75)$$

For $N_s = 6$, $N_m = 4$ and $P_{\rm sp}(1) = 0.01$, we get from Eq. (75) $P_{\rm Dsp}^{\rm fin}(3 \text{ of } 5|1) = 9.85 \times 10^{-8}$. This value is within the range of typical probabilities of false alarm (in the presence of receiver noise) used in designing radar systems. Thus, the "m-of-n" rule in computing the overall correlation for sets of correlated plots is an efficient remedy for eliminating false detections caused by the sea spikes.

A detailed description of the proposed new method is provided in the Appendix.

4. CONCLUSION

This paper has introduced a new method for eliminating false detections in coherent radars due to sea spikes. The proposed method overcomes the drawbacks of the state-of-the-art methods and exhibits essentially improved performance over the latter. The comparative performance analysis has shown that the proposed new method:

- Efficiently eliminates false detections due to the sea spikes by using the "m-of-n" detection strategy in computing the overall correlation.
- Radically improves detection performance for targets of interest through the adequate determination of the extent of correlation windows for radar plot matching in the scan-to-scan data processing.
- Provides higher precision of radial velocity estimation, especially in the presence of sea clutter; this increases the probability of correct matching for plots and, finally, the probability of detection for targets of interest.
- Decreases the number of false detections by providing an essential reduction in the angular extent of the correlation windows.
- Provides reliable detection performance for targets of interest when radial velocity measurements are ambiguous; the prior art methods collapse in such situations.

APPENDIX A. DETAILED DESCRIPTION OF THE PROPOSED METHOD

This description assumes a coherent radar covering a surveillance area in subsequent scans of duration T_{scan}, wherein the radar transmits waveforms and receives returns during a coherent processing interval (CPI). These radar returns contain information on a radar scene within a particular azimuth cell associated with each current CPI in turn.

The proposed new method comprises the following steps.

1. Performing coherent Doppler processing, wherein the input is raw CPI data in the form of a complex-valued fast/slow time data matrix of size M-by-N that represents radar returns received within each current CPI. The output is a complex-valued Range-Doppler data matrix of size M-by-N that represents all radar-available information on a radar scene associated with the current CPI, where M and N is the number of range cells and Doppler bins, respectively.

2. Generating a real-valued Range/Doppler data matrix of size M-by-N from the complex-valued Range-Doppler data matrix from step 1 by computing magnitude-squared value for each element in this complex-valued matrix.

3. Performing CFAR detection using the real-valued Range/Doppler data matrix from step 2. For each range cell, at which at least one Doppler sample is detected, storing in memory the corresponding range cell index and data required for fine Doppler estimation. These data are extracted from the row corresponding to the said range cell index in the complex-valued Range-Doppler data matrix in step 1.

4. For each range cell index associated with detections reported in step 3:

- Performing fine Doppler estimation using the corresponding required data stored in step 3 and computing the radial velocity estimate V and the range estimate R associated with the range cell index.

- Storing in memory the estimates V, R, a value of the maximum magnitude among all the detected Doppler samples associated with the range cell index, and the azimuth cell index α of the corresponding CPI.

5. Repeating steps 1–4 for all consecutive CPIs over the entire antenna scan, i.e., for all azimuth cells associated with these CPIs, and collecting in memory the said range, velocity, azimuth, and magnitude data stored in step 4 during the entire antenna scan.

6. Generating radar plots using the range, velocity, azimuth, and magnitude data accumulated in the memory during the entire antenna scan.

7. Storing in the memory all the plots generated in the n-th current scan and each of the $N_s - 1 \geq 2$ successive previous scans that include the $(n-1)$-th, ..., $(n - N_s + 1)$-th scans.

8. Identifying a set of the correlated plots associated with each i-th plot $P_{ni}(R_i, V_i, \alpha_i)$ $(i = 1, 2, \ldots)$ in the n-th current antenna scan by performing the plot matching process for the i-th initial plot with plots from the $N_s - 1$ successive previous scans.

In step 8, the plot matching process starts from initializing a set of the correlated plots associated with the i-th plot as $SCP_i = \{P_{ni}\}$ and generating an initial correlation window (ICW) for matching the i-th plot $P_{ni}(R_i, V_i, \alpha_i)$ with plots $P_{n-1j}(R_j, V_j, \alpha_j)$ in the $(n-1)$-th scan. The parameters of the ICW are:

- Range position of the center:
$$R_b = R_i - V_i T_{scan}.$$

- Half range extent:
$$LR_a = 3\sqrt{\sigma_R^2 + \sigma_V^2 T_{scan}^2} + 3\sigma_R.$$

where σ_R is the standard deviation of the range centroider and σ_V is a standard deviation of the velocity centroider.

- Azimuth position of the center:
$$A_b = \alpha_i.$$

- Half azimuth extent:
$$LA_{ai} = \left\lceil \frac{\operatorname{atan}\left(\frac{|V_{\mathrm{crmax}}|T_{scan}}{R_{\mathrm{bmin}}}\right)}{\theta_3} \right\rceil N_{sw} + \lceil 3\beta \rceil N_{sw},$$

where $|V_{\mathrm{crmax}}| = \sqrt{V_{\max}^2 - \check{V}^2}$ with $\check{V} = |V_i| - 6\sigma_V$ if $|V_i| > 6\sigma_V$, and $\check{V} = 0$ if $|V_i| \le 6\sigma_V$, N_{sw} is the number of sliding windows within the 3 dB antenna beamwidth θ_3, $R_{\mathrm{bmin}} = R_b - LR_a$, if $R_b > LR_a$, and $R_{\mathrm{bmin}} = R_b$, if $0 < R_b \le LR_a$. The value of parameter β is determined from the equation $\sigma_\alpha = \beta\theta_3$.

After having defined the ICW, the matching process performs the following sub-steps:

8.1 Selecting the plots that fall into the specified ICW, that is, their azimuth and range centroids meet the conditions

$$\alpha_j \in \left[\tilde{A}_L, \tilde{A}_U\right] \text{ and } R_b - LR_a \le R_j \le R_b + LR_a,$$

where

$$\tilde{A}_L = \begin{cases} A_L, & \text{if } 0 \le A_L < N_{az} \\ A_L - N_{az}, & \text{if } A_L \ge N_{az} \\ A_L + N_{az}, & \text{if } A_L < 0 \end{cases} \text{ and } \tilde{A}_U = \begin{cases} A_U, & \text{if } 0 \le A_U < N_{az} \\ A_U - N_{az}, & \text{if } A_U \ge N_{az} \\ A_U + N_{az}, & \text{if } A_U < 0 \end{cases}$$

with $A_L = A_b - LR_{ai}$ and $A_U = A_b + LR_{ai}$, respectively, and N_{az} is the total number of azimuth cells within the full 360° azimuth coverage.

The plots that meet these conditions constitute a set of the selected plots

$$P_{n-1j_p}\left(R_{j_p}, V_{j_p}, \alpha_{j_p}\right), \quad p = 1, 2, \ldots, P.$$

8.2 Determining those plots in the set of the selected plots that meet the velocity matching condition

$$V_i - 6\sigma_V \le V_{j_p} \le V_i + 6\sigma_V$$

The plots that meet this velocity matching condition constitute a set of the matched plots

$$P_{n-1j_g}\left(R_{j_g}, V_{j_g}, \alpha_{j_g}\right), \quad g = p_1 < p_2 < \ldots < p_G, G \le P.$$

8.3 Identifying such a plot $P_{n-1j_{\tilde{g}}}(R_{j_{\tilde{g}}}, V_{j_{\tilde{g}}}, \alpha_{j_{\tilde{g}}})$ in the set of the matched plots that minimizes the overall matching criterion $\mathcal{F}$, such as

$$\mathcal{F} = (V_i - V_{j_{\tilde{g}}})^2 \to \min$$

or of a more general form such as

$$\mathcal{F} = \frac{(R_b - R_{j_{\tilde{g}}})^2}{\sigma_{RV}^2} + \frac{(V_i - V_{j_{\tilde{g}}})^2}{\sigma_V^2} \to \min$$

where $\sigma_{RV}^2 = \sigma_R^2 + \sigma_V^2 T_{scan}^2$.

8.4 Including the plot $P_{n-1j_{\tilde{g}}}\left(R_{j_{\tilde{g}}}, V_{j_{\tilde{g}}}, \alpha_{j_{\tilde{g}}}\right)$ in the set of correlated plots SCP_i associated with the i-th initial plot $P_{ni}\left(R_i, V_i, \alpha_i\right)$: $SCP_i = \{P_{ni}P_{n-1j_{\tilde{g}}}\}$.

If the said set of selected plots or the said set of matched plots in the $(n-1)$-th scan is empty, then the matching process defines new ICW parameters for the $(n-2)$-th scan as

- Range position of the center:
$$R_b = R_i - V_i(2T_{scan})$$

- Half range extent:
$$LR_a = 3\sqrt{\sigma_R^2 + \sigma_V^2(2T_{scan})^2} + 3\sigma_R.$$

- Azimuth position of the center:
$$A_b = \alpha_i.$$

- Half azimuth extent:
$$LA_{ai} = \left\lceil \frac{\mathrm{atan}\left(\frac{|V_{\mathrm{crmax}}|(2T_{scan})}{R_{\mathrm{bmin}}}\right)}{\theta_3} \right\rceil N_{sw} + \lceil 3\beta \rceil N_{sw},$$

and then repeats the sub-steps 8.1–8.4 for the plots $P_{n-2j}(R_j, V_j, \alpha_j)$ in the $(n-2)$-th scan using
in sub-step 8.3 the updated variance $\sigma_{RV}^2 = \sigma_R^2 + \sigma_V^2 (2T_{scan})^2$.

The matching process repeats sub-steps 8.1–8.4, recomputing the ICW parameters and the variance σ_{RV}^2 at each repetition until the first correlated plot is found. Once the said correlated plot is found in the $(n-s_1)$-th scan, $s_1 \in [1, 2, \ldots, N_s - 1]$, the said set of the correlated plots is updated as $SCP_i = \{P_{ni}, P_{n-s_1 j_{\tilde{g}}}\}$, and then the plot matching process continues for the $(n-s_1-1)$-th scan using adaptive correlation windows.

If no correlated plots in all $N_s - 1$ successive previous scans are found, the process starts plot matching for the $(i+1)$-th plot $P_{ni+1}(R_{i+1}, V_{i+1}, \alpha_{i+1})$ in the n-th current antenna scan.

Once the set of correlated plots $SCP_i = \{P_{ni}, P_{n-s_1 j_{\tilde{g}}}\}$ is generated, the plot matching process computes an adaptive correlation window (ACW) for matching the plot $P_{n-s_1 j_{\tilde{g}}}(R_{j_{\tilde{g}}}, V_{j_{\tilde{g}}}, \alpha_{j_{\tilde{g}}})$ with plots $P_{n-s_1-1k}(R_k, V_k, \alpha_k)$ in the $(n-s_1-1)$-th scan. The parameters of this ACW are:

- Range position of the center:
$$R_b = R_{j_{\tilde{g}}} - V_{j_{\tilde{g}}} T_{scan}$$

- Half range extent:
$$LR_a = 3\sqrt{\sigma_R^2 + \sigma_V^2 T_{scan}^2} + 3\sigma_R$$

- Azimuth position of the center:
$$A_b = \tilde{\alpha}_b$$

where
$$\tilde{\alpha}_b = \begin{cases} \alpha_b, & \text{if } 0 \leq \alpha_b < N_{az} \\ \alpha_b - N_{az}, & \text{if } \alpha_b \geq N_{az} \\ \alpha_b + N_{az}, & \text{if } \alpha_b < 0 \end{cases}.$$

with α_b being computed as
$$\alpha_b = \alpha_{j_{\tilde{g}}} + \tilde{\alpha}_{cr}/s_1,$$

wherein
$$\tilde{\alpha}_{cr} = \begin{cases} \Delta\alpha_1, & \text{if } \Delta\alpha_1 \leq \Delta\alpha_2 \\ -\Delta\alpha_2, & \text{if } \Delta\alpha_1 > \Delta\alpha_2 \end{cases}$$

with
$$\Delta\alpha_1 = mod(\alpha_i - \alpha_{j_{\tilde{g}}}, N_{az}) \text{ and } \Delta\alpha_2 = mod\left(\alpha_{j_{\tilde{g}}} - \alpha_i, N_{az}\right).$$

- Half azimuth extent:
$$LA_a^{adp} = \left\lceil 3\left(\sqrt{\frac{(d+h)^2 + h^2}{h^2}} + 1\right)\beta\right\rceil N_{sw}$$

with $d = s_1$, $h = 1$.

After having defined this ACW, the plot matching process performs the following sub-steps:

8.5 Selecting the plots that fall into the said ACW, that is, their azimuth and range centroids, respectively meet the conditions
$$\alpha_k \in \left[\tilde{A}_L, \tilde{A}_U\right] \text{ and } R_b - LR_a \leq R_k \leq R_b + LR_a,$$

where
$$\tilde{A}_L = \begin{cases} A_L, & \text{if } 0 \leq A_L < N_{az} \\ A_L - N_{az}, & \text{if } A_L \geq N_{az} \\ A_L + N_{az}, & \text{if } A_L < 0 \end{cases} \text{ and } \tilde{A}_U = \begin{cases} A_U, & \text{if } 0 \leq A_U < N_{az} \\ A_U - N_{az}, & \text{if } A_U \geq N_{az} \\ A_U + N_{az}, & \text{if } A_U < 0 \end{cases}$$

with $A_L = \tilde{\alpha}_b - LA_a^{adp}$ and $A_U = \tilde{\alpha}_b + LA_a^{adp}$, respectively.

The plots that meet these conditions constitute a set of the selected plots
$$P_{n-s_1-1k_l}\left(R_{k_l}, V_{k_l}, \alpha_{k_l}\right), \quad l = 1, 2, \ldots, L.$$

8.6 Determining those plots in the said set of the selected plots that meet the velocity matching condition

$$V_{j_{\tilde{g}}} - 6\sigma_V \le V_{k_l} \le V_{j_{\tilde{g}}} + 6\sigma_V$$

The plots that meet this velocity matching condition constitute a set of the matched plots

$$P_{n-s_1-1k_u}\left(R_{k_u}, V_{k_u}, \alpha_{k_u}\right), \quad u = l_1 < l_2 < \ldots < l_U, U \le L.$$

8.7 Identifying such a plot $P_{n-s_1-1k_{\tilde{u}}}(R_{k_{\tilde{u}}}, V_{k_{\tilde{u}}}, \alpha_{k_{\tilde{u}}})$ in the set of the matched plots that minimizes the overall matching criterion $\mathcal{F}$, such as

$$\mathcal{F} = (V_{j_{\tilde{g}}} - V_{k_{\tilde{u}}})^2 \to \min$$

or of a more general form such as

$$\mathcal{F} = \frac{(R_b - R_{k_{\tilde{u}}})^2}{\sigma_{RV}^2} + \frac{(\tilde{\alpha}_b - \alpha_{k_{\tilde{u}}})^2}{\sigma_A^2} + \frac{(V_{j_{\tilde{g}}} - V_{k_{\tilde{u}}})^2}{\sigma_V^2} \to \min$$

where $\sigma_{RV}^2 = \sigma_R^2 + \sigma_V^2 T_{scan}^2$ and $\sigma_A^2 = \frac{(d+h)^2 + h^2}{d^2}(\beta N_{sw})^2$ with $d = s_1$ and $h = 1$.

8.8 Including the plot $P_{n-s_1-1k_{\tilde{u}}}(R_{k_{\tilde{u}}}, V_{k_{\tilde{u}}}, \alpha_{k_{\tilde{u}}})$ in the set of the correlated plots SCP_i associated with the i-th initial plot $P_{ni}(R_i, V_i, \alpha_i)$:

$$SCP_i = \{P_{ni}, P_{n-s_1 j_{\tilde{g}}}, P_{n-s_1-1k_{\tilde{u}}}\}.$$

If the set of selected plots or the set of matched plots for the $(n - s_1 - 1)$-th scan is empty, then the matching process defines new ACW parameters for the $(n - s_1 - 2)$-th scan as
   - Range position of the center:

$$R_b = R_{j_{\tilde{q}}} - V_{j_{\tilde{g}}}(2T_{scan})$$

   - Half range extent:

$$LR_a = 3\sqrt{\sigma_R^2 + \sigma_V^2(2T_{scan})^2} + 3\sigma_R$$

   .
   - Azimuth position of the center:

$$A_b = \tilde{\alpha}_b$$

where

$$\tilde{\alpha}_b = \begin{cases} \alpha_b, & \text{if } 0 \le \alpha_b < N_{az} \\ \alpha_b - N_{az}, & \text{if } \alpha_b \ge N_{az} \\ \alpha_b + N_{az}, & \text{if } \alpha_b < 0 \end{cases}$$

with α_b being computed as

$$\alpha_b = \alpha_{j_{\tilde{g}}} + 2\tilde{\alpha}_{cr},$$

wherein

$$\tilde{\alpha}_{cr} = \begin{cases} \Delta\alpha_1, & \text{if } \Delta\alpha_1 \le \Delta\alpha_2 \\ -\Delta\alpha_2, & \text{if } \Delta\alpha_1 > \Delta\alpha_2 \end{cases}$$

with $\Delta\alpha_1 = mod(\alpha_i - \alpha_{j_{\tilde{g}}}, N_{az})$ and $\Delta\alpha_2 = mod\left(\alpha_{j_{\tilde{g}}} - \alpha_i, N_{az}\right)$.
   - Half azimuth extent:

$$LA_a^{adp} = \left\lceil 3\left(\sqrt{\frac{(d+h)^2 + h^2}{h^2}} + 1\right)\beta \right\rceil N_{sw}$$

with $d = s_1$, $h = 2$ and then repeats sub-steps 8.5–8.8 for plots $P_{n-s_1-2r}(R_r, V_r, \alpha_r)$ from the $(n - s_1 - 2)$-th scan using in sub-step 8.7 the updated variances: $\sigma_{RV}^2 = \sigma_R^2 + \sigma_V^2(2T_{scan})^2$ and $\sigma_A^2 = \frac{(d+h)^2 + h^2}{d^2}(\beta N_{sw})^2$ with $d = s_1$ and $h = 2$.

The plot matching process repeats sub-steps 8.5–8.8, recomputing the ACW parameters and the variances σ_{RV}^2 and σ_A^2 (with properly redefined parameters d and h) at each repetition, until the first correlated plot is found. Once the said correlated plot is found at the $(n - s_2)$-th scan, $s_2 \in [s_1 + 1, s_1 + 2, \ldots, N_s - 1]$ the matching process updates the set of the correlated plots as $SCP_i = \left\{ P_{ni}, P_{n-s_1 j_{\tilde{g}}}, P_{n-s_2 r_{\tilde{h}}} \right\}$ and then continues plot matching for the $(n - s_2 - 1)$-th scan and further up to the $(n - N_s + 1)$-th scan using properly redefined adaptive correlation windows. Whenever a new correlated plot is found, the set of the correlated plots is updated so that the finally updated set of the correlated plots associated with the i-th initial plot $P_{ni}(R_i, V_i, \alpha_i)$ is

$$SCP_i = \left\{ P_{ni}, P_{n-s_1 j_{\tilde{g}}}, P_{n-s_2 r_{\tilde{h}}}, \ldots, P_{n-s_{K_i} t_{\tilde{u}}} \right\}$$

wherein the total number of the correlated plots is $N_{icor} = K_i + 1$, $K_i \le N_s - 1$.

Once the set of the correlated plots SCP_i is finally updated, the plot matching process starts for the $(i+1)$-th plot $P_{ni+1}(R_{i+1}, V_{i+1}, \alpha_{i+1})$ in the n-th current antenna scan.

9. Computing the value of overall correlation for each i-th set of the correlated plots found in step 8. If the said value exceeds a predefined threshold, then the initial plot associated with the i-th set of correlated plots is stored in memory for further processing and visualization on a radar display. Otherwise, the said initial plot is retained for processing in step 10.

In step 9, one can compute the overall correlation value using the "$(N_m - 1)$-of-$(N_s - 1)$" rule $(N_m \le N_s)$, with the fixed first detection associated with the initial plot in the n-th current scan. In this rule, $N_m - 1$ is the positive integer detection threshold for the number of detected and correctly matched plots within the $N_s - 1$ successive antenna scans before the n-th current scan.

10. Repeating steps 8 and 9 for each plot retained in step 9 using modified velocity centroids. The modifications are to detect targets that have been (presumably) missed due to ambiguous velocity measurements.

Step 10 comprises the following sub-steps for each r-th initial plot $P_{nr}(R_r, V_r, \alpha_r)$ retained at step 9 in a set of retained plots:

10.1 Set $k = 1$, where the parameter k is the index of the ambiguous velocity interval.

10.2 Compute modified maximum velocity as

$$V'_{\max} = V_{\max} + k v_{ua},$$

where $v_{ua} = \frac{\lambda PRF}{2}$ with λ being the wavelength and PRF being the pulse repetition frequency, and two modified estimates of the velocity centroid for the said r-th initial plot as

$$V_{r1} = V_r + k v_{ua}$$
$$V_{r2} = V_r - k v_{ua}$$

10.3 Repeat step 8 to identify a new set of the correlated plots using in the plot matching process
- Modified maximum velocity $V'_{\max}$.
- Assumed unambiguous estimate of the velocity centroid of the said r-th initial plot V_{r1}.
- Assumed unambiguous estimates of the velocity centroids for all plots that fall within correlation windows generated in the $N_s - 1$ successive previous scans

$$V_{q1} = V_q + k v_{ua}, \quad q = 1, 2, \ldots$$

where V_q, $q = 1, 2, \ldots$ stands for the probably ambiguous initial estimates of the velocity centroids for all plots that fall within correlation windows generated in the $N_s - 1$ successive previous scans.

10.4 Repeat step 9 for a new set of the correlated plots generated in sub-step 10.3.

10.5 If the r-th initial plot associated with a new set of the correlated plots generated in sub-step 10.4 is stored in memory for further processing and visualization or if the r-th initial plot is retained for re-matching after repeating sub-step 10.4 with the modified velocity centroid estimates V_{r2}, go to sub-step 10.6. Otherwise, repeat sub-steps 10.3–10.5 using in the plot matching process V_{r2} instead of V_{r1} and $V_{q2} = V_q - k v_{ua}$ instead of V_{q1}, $q = 1, 2, \ldots$.

10.6 Set $k = k + 1$. If $k \le k_{\max}$, where $k_{\max}$ is the maximum integer value of $k(k_{\max} \ge 1)$, repeat sub-steps 10.2–10.5; otherwise, discard all the plots remaining in a set of the retained plots.

REFERENCES

1. Richards, M. A., J. A. Scheer, and W. A. Holm (eds.), *Principles of Modern Radar — Vol. I, Basic Principles*, SciTech Publishing, Raleigh, NC, 2010.

2. Skolnik, M. I., *Radar Handbook*, 3rd Edition, McGraw-Hill, New York, 2008.

3. Ward, K. D., T. Robert, and W. Simon, *Sea Clutter: Scattering, the K Distribution and Radar Performance*, The Institution of Engineering and Technology, London, 2006.

4. Rosenberg, L., "Sea-spike detection in high grazing angle X-band sea-clutter," *IEEE Transactions on Geoscience and Remote Sensing*, Vol. 51, No. 8, 4556–4562, August 2013.

5. Rosenberg, L., "Persistent sea-spike detection in medium grazing angle X-band sea-clutter," *Proc. 9th European Conf. on Synthetic Aperture Radar, EUSAR 2012*, 203–206, Nuremberg, Germany, April 23–26, 2012.

6. Duk, V., L. Rosenberg, and B. W.-H. Ng, "Target detection in sea-clutter using stationary wavelet transform," *IEEE Transactions on Aerospace and Electronic Systems*, Vol. 53, No. 3, 1136–1146, June 2017.

7. Rosenberg, L., K. Venkataraman, and C. Jenke, "Target detection in medium grazing angle sea clutter using scan to scan processing," *Proc. Int. Conf. Radar*, 1–5, Toulon, France, September 23–27, 2019.

8. Guan, J., N.-B. Liu, Y. Huang, and Y. He, "Fractal Poisson model for target detection within spiky sea clutter," *IEEE Geoscience and Remote Sensing Letters*, Vol. 10, No. 2, 411–415, March 2013.

9. Li, Yu., P. Xie, Z. Tang, T. Jiang, and P. Qi, "SVM-based sea-surface small target detection: A false alarm controllable approach," *IEEE Geoscience and Remote Sensing Letters*, Vol. 16, No. 8, 1225–1229, August 2019.

10. Bell, K. L., H. L. Van Trees, B. R. Osborn, and R. E. Zarnich, "A range-coherent model for discriminating targets and wave clutter in high range resolution surface radar," *Proc. IEEE Radar Conf. RadarCon 2011*, 740–745, Kansas City, MO, USA, May 23–27, 2011.

11. Gallone, S., F. Amato, A. Brelati, et al., US Patent 9,041,597 B2, May 26, 2015.

12. Kononov, A. A., J. H. Kim, J. K. Kim, and G. Kim, "A new class of adaptive CFAR methods for nonhomogeneous environments," *Progress In Electromagnetics Research B*, Vol. 64, 145–170, 2015.

13. Kononov, A. A., D. Kim, and H. S. Kim, Korean Patent 10-1871874, June 21, 2018.

14. Kononov, A. A. and J. Kim, "Efficient elimination of multiple-time-around detections in pulse-Doppler radar systems," *Progress In Electromagnetics Research B*, Vol. 71, 55–76, 2016.

15. Kononov, A. A., D. Kim, and S.-H. Choi, Korean Patent 10-1902833, September 20, 2018.